J. Fluid Mech. (1998), *vol.* 366, *pp.* 33–85. Printed in the United Kingdom

Instabilities of conical flows causing steady bifurcations

By VLADIMIR SHTERN AND FAZLE HUSSAIN
Department of Mechanical Engineering, University of Houston, Houston, TX77204-4792, USA

(Received 12 December 1995 and in revised form 22 December 1997)

A new stability approach is developed for a wide class of strongly non-parallel axisymmetric flows of a viscous incompressible fluid. This approach encompasses all conical flows, and all steady and weakly unsteady disturbances, while prior studies were limited to specific flows and particular disturbances. A specially derived form of the Navier–Stokes equations allows the exact reduction of the linear stability problem to a system of ordinary differential equations. We found that disturbances originating at the boundaries of a similarity region cause a variety of steady bifurcations. Consideration of the still fluid allows disturbances to be classified into inner, outer and global modes, depending on the boundary conditions perturbed. Then we identify and study modes which cause bifurcation as the Reynolds number increases. The study provides improved understanding of (*a*) azimuthal symmetry breaking, (*b*) genesis of swirl, (*c*) onset of heat convection, (*d*) hydromagnetic dynamo, (*e*) hysteretic transitions, and (*f*) jump flow separation. We also discover and analyse two new bifurcations: (*g*) fold catastrophes and (*h*) appearance of radial oscillations in swirl-free jets. The stability analysis reveals that bifurcations (*a*), (*c*) and (*f*) are caused by inner perturbations, bifurcations (*b*), (*d*), (*e*) and (*g*) by outer perturbations, and bifurcation (*h*) by global perturbations. We deduce amplitude equations to describe the nonlinear spatiotemporal development of disturbances near the critical Reynolds numbers for (*b*) and (*g*). Disturbances switching between the basic and secondary steady states are found to grow monotonically with time.

CONTENTS

1. Introduction

1.1. *Conically similar flows*

This paper develops a new approach for stability analysis of steady-state bifurcations in conically similar flows of a viscous incompressible fluid. Conical similarity is a feature of a wide family of solutions of the Navier–Stokes, heat, diffusion and magnetohydrodynamic (MHD) equations. The family includes planar vortex-sink and Jeffery–Hamel flows (Batchelor 1967), swirl-free jets (Schlichting 1933; Landau 1944), swirling jets (Long 1961; Serrin 1972), swirling flows (Yih *et al.* 1982), Marangoni convection (Bratukhin & Maurin 1967), thermal convection (Schneider 1981) and electro-vortex flows (Bojarevics *et al.* 1989). This list of topics is incomplete, and only a handful of references are cited here. For reviews and general features of the conical solutions see, e.g. Pillow & Paull (1985) and Wang (1991).

In conically similar flows, velocity $\boldsymbol{v}$ and pressure p have the representation,

$$\boldsymbol{v} = \nu r^{-1}\,\boldsymbol{V}(\theta,\phi), \quad p = p_\infty + \rho\nu^2 r^{-2} q(\theta,\phi), \tag{1a}$$

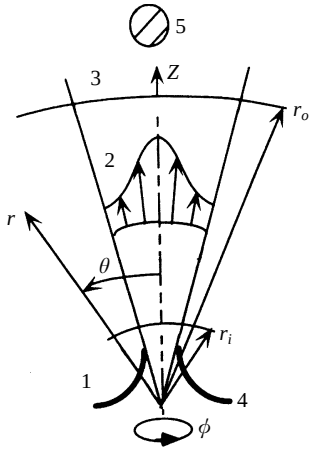

FIGURE 1. Schematic of the similarity region in the round jet.

where (r, θ, ϕ) are the spherical coordinates (figure 1), ρ is the density, and ν is the kinematic viscosity. Substituting (1*a*) and multiplying all terms by r^{-3}, one exactly reduces the Navier–Stokes equations (NSE) to a set of equations for dimensionless functions $\boldsymbol{v}$ and q, which replace velocity and pressure. The set becomes a system of ordinary differential equations (ODE) for axisymmetric flows. Representations for temperature, concentration and magnetic induction similar to that for velocity yield analogous reduction of the heat, diffusion and MHD equations.

Note that all terms of NSE (except time derivatives) remain in the reduced equations, and thus both diffusion and convection contribute to the ODE. These nonlinear ODEs describe many important effects observed in practical flows including: development of boundary layers, inner viscous layers, solution non-uniqueness, flow separation, vortex breakdown, collapse (self-focusing of axial and angular momenta), swirl generation and magnetic dynamo. On the other hand, being drastically simpler than NSEs, the ODEs allowed a detailed analysis and even provide analytical solutions which help to clarify the essential physical mechanisms involved in the above-mentioned effects.

Conical solutions are widely used for modelling technological and natural flows. Schlichting (1979) applied his solution for turbulent round jets. Taylor (1950) posed a conical problem for a liquid fuel motion in a swirl atomizer. Goldshtik (1960) found his paradoxical solution by investigating the wall effect in vortex reactors. Long (1961), Serrin (1972) and Sozou (1992) modelled tornadoes by conical flows. Wang (1991) used Squire's (1952) solution to imitate the oceanic motion induced by a tanker crash. Bojarevics *et al.* (1989) studied MHD conical flows for applications in electro-metallurgy and plasmatrons. Conical solutions have been used to model flows in electrosprays (Shtern & Barrero 1995*a*) and vortex suction devices (Shtern & Hussain 1996).

Turbulence modelling

Since most of the practical flows mentioned are turbulent, their modelling includes interpreting of ν as the uniform eddy viscosity ν_t (Schlichting 1979; Serrin 1972; Burggraf & Foster 1977). The r-independence results from conical similarity (which is observed not only in the mean velocity field but also in turbulent fluctuations): ν_t is the product of velocity and length scales of turbulent fluctuations – the length and velocity scales are proportional to r and r^{-1} in conical flows. The ϕ-independence follows from axisymmetry. In general, ν_t is a function of the polar angle θ but this dependence can

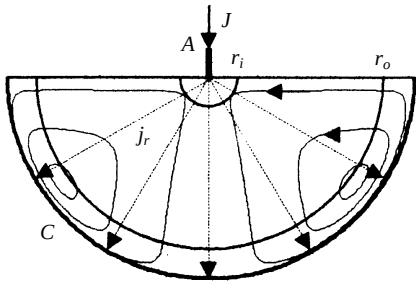

FIGURE 2. Schematic of the similarity region, $r_i < r < r_o$, in the confined flow.

be ignored in rough approximations, especially if the flow is slender. For example, uniform ν_t for the round turbulent jet leads to satisfactory agreement with experiment (Schlichting 1979).

Invariants

Conical similarity indicates that such flows depend on a few control parameters only. Far from boundaries, a flow is typically oblivious of most of the constraints posed by boundary conditions; however, the flow depends on invariant characteristics, such as the flow force and circulation. This feature leads to similarity of many practical flows, and justifies and helps to obtain similarity solutions. In particular, Schlichting (1933) and Landau (1944) deduced their analytical solutions by exploiting the invariance of the flow force, and Long (1961) generalized this approach for swirling jets having r-independent circulation.

Similarity regions

Typically, similarity occurs in a part of the flow region away from boundaries. Figure 1 shows this schematically for a round jet. Similarity is absent in region 1 (near nozzle 4) and region 3 (near ambient body 5 or bounding wall) but occurs in the intermediate region 2, $r_i < r < r_o$. A necessary condition for similarity to occur is $r_o/r_i \gg 1$, where r_i is proportional to the nozzle radius and r_o is the typical distance from the nozzle to ambient bodies. The entrainment flow induced by a jet or a plume can be conically similar as well (Schneider 1981; Schneider, Zauner & Bohm 1987).

Similarity regions exist also in confined flows. Figure 2 shows the flow studied both experimentally and numerically by Bojarevics *et al.* (1989). In the experiment, mercury filling a hemispherical copper container is in circulatory meridional motion (the closed curves represent typical streamlines) driven by the electric current (rays) from electrode A to wall C. Bojarevics *et al.* revealed that this steady axisymmetric flow is close to that described by the conically similar solution (Sozou 1971) except in the vicinities of A and C ($r < r_i$ and $r > r_o$ in figure 2). As the Reynolds number increases, the thickness of these vicinities (typical of boundary layers) decreases.

Conditions at boundaries of similarity regions

It follows from (1 *a*) that conical flows satisfy the relation $\partial V/\partial r = 0$, $V = r\boldsymbol{v}$. Using this relation as the boundary condition,

$$\partial V/\partial r = 0 \quad \text{at} \quad r = r_i, \quad r = r_o, \tag{1 b}$$

one can view conical flows as solutions of NSEs in a bounded three-dimensional region. Also, conditions,

$$V(r_i) = V(r_o), \quad \partial V/\partial r(r_i) = \partial V/\partial r(r_o), \tag{1 c}$$

are consistent with (1*a*). We apply (1*b*, *c*) to study transitions between conical solutions in §7.

Inner and outer disturbances

In practical flows, (1*a*) is valid inside a similarity region, but real conditions at $r = r_i$ and $r = r_o$ differ from (1*b*, *c*) and thus generate disturbances. The question is how these disturbances influence the flow in $r_i \leqslant r \leqslant r_o$. The similarity flow is unstable if disturbances increase as one moves from $r = r_i$ or $r = r_o$ to within the similarity region. This paper addresses particularly this point: it considers how inner (i.e. given at $r = r_i$) and outer (at $r = r_o$) disturbances influence conical flows as a function of control parameters, say, Reynolds number *Re*.

First, we consider time-independent infinitesimal disturbances whose normal modes are proportional to r^α where $\alpha = \alpha_r + \mathrm{i}\alpha_i$ are eigenvalues to be found. As is typical of the spatial instability, there is an infinite set of eigenvalues with $\alpha_r < 0$ and another infinite set with $\alpha_r > 0$. This is due to the fact that NSEs are elliptic: both the inner and outer boundary conditions influence the solution. For stable similarity flows, superposition Σ_- of the modes with $\alpha_r < 0$ is the contribution of disturbances given at the inner boundary, $r = r_i$, which decay as *r* increases, while superposition Σ_+ of the modes with $\alpha_r \geqslant 0$ is the contribution of disturbances given at the outer boundary, $r = r_o$, and decaying as *r* decreases. The existence of eigenvalues with both $\alpha_r < 0$ and $\alpha_r > 0$ need not imply any instability. Instability and bifurcation of new solutions occur only when α_r changes its sign at $Re = Re_{cr}$. The 'inner-mode instability' occurs when $\alpha_r < 0$ in $0 \leqslant Re < Re_{cr}$ and $\alpha_r > 0$ for $Re > Re_{cr}$, while the 'outer-mode instability' occurs when $\alpha_r > 0$ in $0 \leqslant Re < Re_{cr}$ and $\alpha_r < 0$ for $Re > Re_{cr}$. We find both the inner and outer instabilities of conical flows induced by steady disturbances in §§4–6. Then we verify the nature of instabilities and bifurcation at $Re = Re_{cr}$ by studying the spatiotemporal nonlinear evolution of growing modes in §7.

Although limited to steady-state bifurcation, this approach can treat many kinds of instabilities observed in practical flows. It has long been established that steady-state bifurcation occurs owing to the thermogravitational and Taylor–Görtler instabilities (Drazin & Reid 1981). Secondary stationary flows also develop owing to the cross-flow instability on swept wings of aircraft and near rotating disks (Gregory, Stuart & Walker 1955). Other examples of steady bifurcation which closely relate to conical flows – azimuthal symmetry breaking, hysteresis, onset of convection, swirl generation and MHD dynamo – are reviewed below.

1.2. *Steady bifurcations in conical flows*

Plane-diffuser flow

The Jeffery–Hamel solution, modelling the diverging flow in a plane diffuser, exists for small, but not for large, $Re = Q/\nu$, *Q* is the flow rate (Hamel 1916). This striking fact is occasioned by the occurrence of a fold catastrophe (merging and disappearance of two solutions) at $Re = Re_f$. At $Re = Re_{cr} < Re_f$, the diverging-flow solution becomes unstable to asymmetric disturbances. In Jeffery–Hamel flow, the fold and the symmetry breaking both result from steady-state subcritical bifurcations (Hooper, Duffy & Moffatt 1982).

Divergent instability

Symmetry breaking in Jeffery–Hamel flows is a specific manifestation of the azimuthal instability occurring in radially diverging flows. This instability is possibly one of the first documented in the literature. Thompson (1855) observed spreading of

alcohol (introduced by a capillary tube) from the centre of the water surface in a wineglass. He found 'by the motion of the powder, one, two, three, or many radial streams flowing outwards from the middle, and other return streams or eddies flowing backwards to the margin of the patch'. Pshenichnikov & Yatsenko (1974) repeated this experiment and photographed the flow patterns. They gradually increased the flow rate and measured the critical flow-rate values at which the number of eddies changes from 2 to 10. The motion becomes unsteady for larger flow-rate values. Shtern & Hussain's (1993) analysis of the axisymmetry breaking showed agreement with the experimental results of Pshenichnikov & Yatsenko. The divergent instability typically leads to steady secondary flows.

Hysteretic transitions

A known problematic feature associated with natural and technological swirling flows is multi-stability, i.e. existence of several stable states for the same values of control parameters. External disturbances or even continuous variation of the control parameters can cause abrupt switching between the states. Hysteretic transitions occur in leading-edge vortices of aircraft (Lowson 1964), in tornadoes (Burggraf & Foster 1977) and in vortex chambers (Goldshtik 1990). This phenomenon corresponds to solution non-uniqueness and fold bifurcations in mathematical models, e.g. inviscid studies of vortex breakdown (Saffman 1992), numerical simulation of viscous swirling flows in a diverging pipe (Beran & Culick 1992), and conical solutions for tornadoes and suction devices (Shtern & Hussain 1996). These folds are also examples of the steady-state instability.

Swirl generation

A striking example of symmetry breaking is the appearance of swirl in swirl-free flows. Bojarevics *et al*. (1989) found experimentally (see § 1.1 and figure 2) that no swirl is observed for the total electric current $J_t < 15$ A, but the meridional motion is accompanied by swirl for $J_t > 15$ A. While the swirl velocity increases with J_t, flow stationarity occurs for a wide range of J_t. A similar effect occurs in conical menisci of electrosprays as electric potential increases (Fernandez de la Mora, Fernandez Feria & Barrero 1991). These effects stimulated research of the swirl development in conical similarity flows. The conical models (although strong idealizations of practical flows) demonstrate an analogous phenomenon – a pitchfork bifurcation of swirl (see §§ 5 and 7.2). Steady-state bifurcation in conical flows also leads to the appearance of a magnetic field in primarily non-magnetic flows and to the onset of heat convection (Goldshtik & Shtern 1993).

Thus, steady bifurcation involves many flow instabilities of practical and fundamental interest. Analysis of growing disturbances helps to clarify the physical mechanisms of these instabilities, but meets some difficulties. Early efforts to overcome these difficulties are reviewed below.

1.3. *Instability of conical flows*

Non-parallelism

The major difficulty in the stability analysis is the strong non-parallelism of conical flows. Classical linear hydrodynamic stability methods address mainly parallel flows, allowing reduction of partial differential equations for disturbances to ODEs such as the Rayleigh and Orr–Sommerfeld equations (Drazin & Reid 1981). Since many practical flows are nearly parallel, most research employs a small-parameter technique,

using different kinds of quasi-parallel approximations. One of the recently improved techniques is the parabolized stability equations (Bertolotti 1995).

Quasi-parallel approach

The quasi-parallel stability approach is an effective tool for studying some conical flows that are nearly parallel, e.g. Jeffery–Hamel flow in a slightly diverging channel and axisymmetric jets consolidated near the axis. Regarding Jeffery–Hamel flow, see e.g. Georgiou & Eagles (1985). Numerous works (Foster 1993; Khorami & Triveli 1994; Ardalan, Draper & Foster 1995; also references therein) have studied the temporal instability of Long's vortex under the quasi-parallel approximation. However, as flow divergence increases (e.g. in wide-angle diffusers), this approximation becomes questionable.

Steady disturbances

A specific feature of conical flows is that their steady instability can be studied without the quasi-parallel approximation (§2.3). This feature was effectively exploited in stability studies of Jeffery–Hamel flow (Dean 1934; Banks, Drain & Zaturska 1988). Drazin, Banks & Zaturska (1995) have also formulated a spatial stability approach for Long's vortex without quasi-parallel approximation.

These earlier approaches were limited to specific conical flows and instabilities. The studies of Jeffery–Hamel flows addressed only two-dimensional disturbances. The approach by Shusser & Weihs (1995) captured three-dimensional disturbances but only for irrotational planar basic flows. The technique of Drazin *et al.* (1995) was limited to flows in a half-space. Studies of the spatial instability addressed only disturbances given at a small r and developing with increasing r. Here, we develop a general and effective method encompassing all conical flows and all types of steady and weakly unsteady disturbances.

Note that the steady instability often occurs at smaller Re than that for the time-oscillatory instability. In particular, this applies to source and sink flows (Shusser & Weihs 1995), and to Jeffery–Hamel flow, except in diffusers of very small angle (Georgiou & Eagles 1985). Observations of secondary steady flows (§1.2) also show that steady-state bifurcation can occur at smaller Re than that at which unsteady flows develop.

The classification of spatial modes into 'inner' and 'outer' is important for understanding the instability mechanism in conical flows. To reveal where the origin of the spatial instability is located, we study the dependence of flow disturbances on Re. If one addresses disturbances at a fixed Re only, an unstable inner mode can be confused with a stable outer mode. To avoid such a confusion, we start with $Re = 0$, considering disturbances of a fluid at rest where the mode classification in unambiguous because of the physical reasoning. After the mode identification, we increase Re looking for the mode – inner or outer – that causes the instability. As Re grows, inner and outer modes can merge; we call such merged modes global.

Summary of the approach

Thus, the goal of this paper is to develop an effective general method for studying the steady instability of conical flows. This involves derivation of a new form of NSEs allowing the exact reduction of the linear stability problem to ODEs (§2), classification of modes into inner and outer based on analytical solutions for disturbances in a fluid at rest (§3), and investigation of the mode behaviour as Re increases. The particular instabilities studied here are fold catastrophes and bifurcation of ln r-periodic steady

states in swirl-free jets (§4), swirl bifurcation (§5) and divergent instability (§6). Then the spatiotemporal evolution of instability modes in the vicinity of $Re = Re_{cr}$ is studied (§7). The new results are discussed in §8 and summarized in §9.

2. Problem formulation

2.1. *New form of the Navier–Stokes equations*

Consider the Navier–Stokes equations (NSE),

$$\partial \boldsymbol{v}/\partial t + (\boldsymbol{v}\cdot\boldsymbol{\nabla})\,\boldsymbol{v} + \boldsymbol{\nabla} p/\rho - \nu \Delta \boldsymbol{v} = 0, \quad \boldsymbol{\nabla}\cdot\boldsymbol{v} = 0,$$

for a viscous incompressible fluid. A steady axisymmetric conical flow having the representation (1*a*) is the 'basic' solution whose stability is studied. We consider flows in a region bounded by an impermeable conical surface, $\theta = \theta_c$. For flows driven by shear stresses given on the cone surface, the tangential velocity is non-zero at $\theta = \theta_c$. For flows driven by body forces, the no-slip condition is satisfied at $\theta = \theta_c$. We consider the entire range, $0 < \theta_c \leqslant 180°$. The basic solution is characterized by Reynolds number *Re*, which will be defined for each problem considered.

The equations for finite-amplitude disturbances $\boldsymbol{u}$ of basic flow $\boldsymbol{v}$ can be written in the form

$$\partial \boldsymbol{u}/\partial t + (\boldsymbol{v}\cdot\boldsymbol{\nabla})\,\boldsymbol{u} + (\boldsymbol{u}\cdot\boldsymbol{\nabla})\,\boldsymbol{v} + \boldsymbol{\nabla} p/\rho - \nu \Delta \boldsymbol{u} + (\boldsymbol{u}\cdot\boldsymbol{\nabla})\,\boldsymbol{u} = 0, \quad \boldsymbol{\nabla}\cdot\boldsymbol{u} = 0,$$

The linear stability theory addresses infinitesimal disturbances for which the term, $(\boldsymbol{u}\cdot\boldsymbol{\nabla})\,\boldsymbol{u}$, is negligible. The $Re = 0$ case means the absence of a basic flow, i.e. $\boldsymbol{v} = 0$ and hence the second and third terms disappear. We mainly consider steady disturbances, $\partial \boldsymbol{u}/\partial t = 0$, except in §7.

To ease the stability analysis, it is convenient to modify both the dependent and independent variables by introducing

$$\left.\begin{aligned} \xi = \ln(r/r_0), \quad x = \cos\theta, \quad \tau = \nu t/r_0^2, \quad u(x,\phi,\xi,\tau) = v_r\, r/\nu, \quad y(x,\phi,\xi,\tau) = v_\theta\, r \sin\theta/\nu, \\ \Gamma(x,\phi,\xi,\tau) = v_\phi\, r \sin\theta/\nu, \quad q(x,\phi,\xi,\tau) = (p - p_\infty)\, r^2/(\rho\nu^2). \end{aligned}\right\} \tag{2}$$

The use of r_0 makes the argument of the logarithmic function and τ dimensionless. However, it will be shown that the results are independent of this lengthscale. Dimensionless functions (u, y, Γ) and q replace the velocity components (v_r, v_θ, v_ϕ) and pressure. (Note that the azimuthal angle ϕ is not transformed.) Substitution of (2) in NSE in the spherical coordinates (see, e.g. Batchelor 1967) yields the system,

$$y_x = u + u_\xi + \Gamma_\phi/(1-x^2), \tag{3a}$$

$$\begin{aligned} (1-x^2)\,u_{xx} = {} & (2x-y)\,u_x - u_{\xi\xi} - u_\xi + u u_\xi - u^2 - 2q + q_\xi \\ & + (\Gamma u_\phi - y^2 - \Gamma^2 - u_{\phi\phi})/(1-x^2) + u_\tau \exp(2\xi) + fr, \end{aligned} \tag{3b}$$

$$\begin{aligned} (1-x^2)\,\Gamma_{xx} = {} & u\Gamma_\xi - y\Gamma_x + \Gamma_\xi - \Gamma_{\xi\xi} - 2u_\phi + q_\phi + (\Gamma\Gamma_\phi - 2xy_\phi - \Gamma_{\phi\phi})/(1-x^2) \\ & + \Gamma_\tau \exp(2\xi), \end{aligned} \tag{3c}$$

$$\begin{aligned} (1-x^2)\,q_x = {} & (1-x^2)\,(u_x - u_{x\,\xi}) - \Gamma_{x\phi} + u y_\xi - y u_\xi - y u + y_\xi - y_{\xi\xi} \\ & + [\Gamma y_\phi - y\Gamma_\phi - x(y^2 + \Gamma^2) - y_{\phi\phi}]/(1-x^2) + y_\tau \exp(2\xi) + f\theta, \end{aligned} \tag{3d}$$

where the subscripts denote differentiation with respect to the corresponding variables. The radial fr and meridional $f\theta$ components of body forces in (3*b*) and (3*d*) will be specified for individual problems. There is no azimuthal component of body forces in the problems considered.

System (3) is a specially derived form of NSE for stability studies of conical flows. The advantage of (3) is that coefficients of its steady form (where $u_\tau = \Gamma_\tau = y_\tau = 0$) depend on only one independent variable, x, as distinct from the coefficients of the classical spherical form of NSE, which depend on two coordinates, r and θ. Solutions of (3) for axisymmetric conical flows, considered here as basic solutions, also depend only on x. Linearization of (3) for steady disturbances of the basic solutions leads to a system whose coefficients, again, depend only on x. Thus, the transformation allows the normal (exponential) form for infinitesimal disturbances with respect to ξ and ϕ when one studies the steady instability of conical flows.

2.2. *Equations for basic flows*

Since basic solutions are rotationally symmetric, the Stokes stream function Ψ can be introduced as $\Psi = \nu r\psi(x)$ for these flows. The dimensionless meridional and radial velocity components then become: $y = -\psi$, $u = -\psi'$ (where $()' \equiv \mathrm{d}()/\mathrm{d}x$). It appears convenient (Goldshtik 1960) to introduce an auxiliary function F (equation (4*b*) serves as the definition of F) instead of q. Then (3) is reduced for the basic flows to the ODE system:

$$(1-x^2)\,\psi' + 2x\psi - \tfrac{1}{2}\psi^2 = F, \quad (1-x^2)\,F''' = 2\Gamma\Gamma' + f_b, \quad (1-x^2)\,\Gamma'' = \psi\Gamma'. \quad (4a\text{–}c)$$

The last term in (4*b*) represents (reduced) body forces. Specific solutions of (4) are described below.

2.3. *Equations for disturbances*

We use the following normal form to study the linear instability of the similarity solutions with respect to steady disturbances:

$$\left.\begin{aligned} u &= u_b(x) + u_d(x)\exp(\alpha\xi + \mathrm{i}m\phi) + \text{c.c.},\\ y &= y_b(x) + y_d(x)\exp(\alpha\xi + \mathrm{i}m\phi) + \text{c.c.},\\ q &= q_b(x) + q_d(x)\exp(\alpha\xi + \mathrm{i}m\phi) + \text{c.c.},\\ \Gamma &= \Gamma_b(x) + \mathrm{i}\Gamma_d(x)\exp(\alpha\xi + \mathrm{i}m\phi) + \text{c.c.}, \end{aligned}\right\} \quad (5)$$

where c.c. denotes complex conjugate terms, m is integer, α is complex, and subscripts b and d indicate functions related, respectively, to the basic flow and to disturbances. Substitution of (5) reduces the linearized version of (3) to

$$y_d' = (1+\alpha)\,u_d - m\Gamma_d/(1-x^2), \quad (6a)$$

$$(1-x^2)\,u_d'' = (2x-y_b)\,u_d' + [(\alpha-2)\,u_b + p_1 - \alpha - \alpha^2]\,u_d - u_b' y_d + (\alpha-2)\,q_d - p_4, \quad (6b)$$

$$(1-x^2)\,\Gamma_d'' = (\alpha u_b + p_5)\,\Gamma_d - y_b\,\Gamma_d' + (\mathrm{i}\Gamma_b' - p_2)\,y_d - 2mu_d + mq_d, \quad (6c)$$

$$(1-x^2)\,q_d' = (1-x^2)(1-\alpha)\,u_d' + [p_5 - (1-\alpha)\,u_b]\,y_d - (1+\alpha)\,y_b\,u_d - xp_4 + m\Gamma_d' + p_3\Gamma_d, \quad (6d)$$

where

$$p_1 = (\mathrm{i}m\Gamma_b + m^2)/(1-x^2), \quad p_2 = 2mx/(1-x^2), \quad p_3 = my_b/(1-x^2),$$

$$p_4 = 2(y_b y_d + \mathrm{i}\Gamma_b\Gamma_d)/(1-x^2), \quad p_5 = \alpha - \alpha^2 + p_1.$$

2.4. *Boundary conditions*

Boundary-value problems are considered for (4) and (6) in the region, $x_c \leqslant x \leqslant 1$, $x_c \geqslant -1$. Boundary conditions applied at $x = x_c$ and $x = 1$ are listed below.

2.4.1. *Velocity boundedness*

The axis of symmetry corresponds to the singularity points, $x = \pm 1$, for (4) and (6). If there is no given singularity on the axis, the solution must be regular at $x = \pm 1$. This leads to the conditions,

$$\psi = \Gamma = F = F' = 0 \quad \text{at} \quad x = 1 \tag{7a}$$

for the basic flows. Owing to the singularities of (4) at $x = 1$, there are four conditions in (7*a*), but there is also an additional parameter $\psi'(1)$ which cannot be found from (4*a*) owing to the 0/0 indeterminacy. Therefore $\psi'(1)$, $\Gamma'(1)$, and $F''(1)$ are parameters which must be adjusted to satisfy the conditions at $x = x_c$.

For velocity disturbances, the boundedness requirement yields at $x = 1$:

$$y_d(1) = \Gamma_d(1) = 0. \tag{7b}$$

It follows from (6*b*),

$$\left.\begin{aligned} &u_d(1) = 0 \quad \text{for} \quad m \neq 0, \\ &f_d \equiv 2u_d'(1) + [(\alpha-2)\,u_b(1) - \alpha - \alpha^2]\,u_d(1) + (\alpha-2)\,q_d(1) = 0 \quad \text{for} \quad m = 0. \end{aligned}\right\} \tag{7c}$$

To start integration from $x = 1$, one also needs $u_d'(1)$, $\Gamma_d'(1)$ and $q_d(1)$. Their values should at first be guessed and can then be adjusted to satisfy the conditions at $x = x_c$. The conditions at $x = x_c$ for different problems studied below.

2.4.2. *No slip*

When the no-slip condition is applied on the cone surface, one obtains

$$\psi = \Gamma = F = 0 \quad \text{at} \quad x = x_c, \tag{8a}$$

$$y_d = \Gamma_d = u_d = 0 \quad \text{at} \quad x = x_c. \tag{8b}$$

2.4.3. *Stress-free boundary*

The shear stresses on the cone surface (as on a free surface of a liquid meniscus) are

$$\tau_{\theta r} = \rho\nu[r^{-1}\partial v_r/\partial\theta + r\partial/\partial r(v_\theta/r)] = \rho\nu^2(r^2\sin\theta)^{-1}[y_\xi - 2y - (1-x^2)\,u_x], \tag{9a}$$

$$\begin{aligned}\tau_{\theta\phi} &= \rho\nu r^{-1}[\sin\theta\partial/\partial\theta(v_\phi/\sin\theta) + (\sin\theta)^{-1}\,\partial v_\theta/\partial\phi] \\ &= -\rho\nu^2(r\sin\theta)^{-2}[(1-x^2)\,\Gamma_x + 2x\Gamma + y_\phi].\end{aligned} \tag{9b}$$

Our study includes basic flows driven by shear stresses given at $x = x_c$. These stresses are fixed as the flows are disturbed. The impermeability and stress-free conditions lead to

$$\psi = \psi'' = (1-x^2)\,\Gamma' + 2x\Gamma = 0 \quad \text{at} \quad x = x_c. \tag{10a}$$

$$y_d = u_d' = (1-x^2)\,\Gamma_d' + 2x\Gamma_d = 0 \quad \text{at} \quad x = x_c. \tag{10b}$$

2.4.4. *Given flow force*

For the Landau, Squire, and Long jets, the axial flow force J is given. To express J in terms of the new variables:

$$J = 2\pi r^2 \int \Pi_{zr}\,\mathrm{d}x = 2\pi\rho\nu^2 J_1, \quad J_1 = \int j\,\mathrm{d}x, \quad \Pi_{zr} = \Pi_{rr}\cos\theta - \Pi_{\theta r}\sin\theta,$$

where the integration range is from x_c to 1, and Π_{ij} is the projection of the flow force per unit area acting on an infinitesimal planar surface with normal vector n_j, on the i-axis. Since

$$\Pi_{rr} = \rho v_r^2 + p - 2\rho\nu r^{-1}\partial v_r/\partial r = \rho\nu^2 r^{-2}[u^2 + q + 2(u - u_\xi)],$$

$$\Pi_{\theta r} = \rho v_r v_\theta - \rho\nu[r\partial/\partial r(v_\theta/r) + r^{-1}\partial v_r/\partial\theta] = \rho\nu^2(r^2\sin\theta)^{-1}[uy - y_\xi + 2y + (1-x^2)\,u_x],$$

we find

$$j = x[u(u+2) + q - 2u_\xi] - y(u+2) + y_\xi - (1-x^2)\,u_x. \tag{11}$$

Relation (11) resembles that used by Shtern & Hussain (1996), where u, y, and q were functions of x only, unlike in (2). The flow force being fixed as the flows are disturbed, disturbances must satisfy the condition

$$J_d = \{(\alpha-2-u_b)\,y_d+[2x(1-\alpha+u_b)-y_b]\,u_d-(1-x^2)\,u_d'+xq_d\}\,\mathrm{d}x = 0. \qquad (12)$$

A similar condition was used by Drazin *et al.* (1995) while studying the stability of Long's vortex. These integral conditions for the flow force here replace the conditions, $\psi'' = 0$ and $u_d' = 0$, in (10).

2.4.5. *Eigenvalue problem*

The conditions for disturbances (e.g. (7*b*, *c*) and (8*b*)) and equations (6) form a closed problem which admits the trivial solution, $u_d = y_d = q_d = \Gamma_d = 0$. To find a non-trivial (eigen) solution for the normal modes, look for (complex) eigenvalues $\alpha = \alpha_r + \mathrm{i}\alpha_i$.

2.5. *Invariant features of the stability problem*

The meridional motions of the basic flows are invariant with respect to the sign of circulation, and the stability problem is invariant to the transformations: {$\Gamma_b \to -\Gamma_b$ and complex conjugation} or {$m \to -m$, $\Gamma_d \to -\Gamma_d$, and complex conjugation}. Therefore, it suffices to consider only $\Gamma_b \geqslant 0$ and $m \geqslant 0$.

For $m = 0$, the stability problem has the analytical solutions,

$$\alpha = 2, \quad q_d \equiv \text{const}, \quad y_d = u_d = \Gamma_d \equiv 0, \qquad (13a)$$

$$\alpha = -1, \quad y_d = \Gamma_d \equiv 0, \quad q_d = 2u_d + C_q, \qquad (13b)$$

where u_d is a solution of (6*b*) satisfying the boundary conditions, and C_q is an arbitrary (non-zero) number. It is clear from (13) that these eigenvalues do not depend on the basic flow and are not related to any instability.

For the appropriate physical interpretation and classification of the normal modes, it is useful to start from the case when the basic state is the fluid at rest. Physical reasoning leads one to expect this state to be stable, which helps in a straightforward classification of the modes. Also, analytical solutions for the fluid at rest (§3) serve as checks for further numerical results in §§4–6.

3. Stability of the fluid at rest

3.1. *Modified equations for disturbances*

To study the response of the fluid at rest to infinitesimal disturbances, we eliminate all terms related to the basic flow in (6). To ease the analysis that follows, it is useful to make the additional transformations,

$$u_n = (1+\alpha)\,u_d, \quad q_n = q_d-(1-\alpha)\,u_d,$$

which reduce (6) to the system,

$$y_d' = u_n - m\Gamma_d/(1-x^2), \qquad (14a)$$

$$(1-x^2)\,u_n'' = 2xu_n' + p_3\,u_n + p_4\,q_n, \qquad (14b)$$

$$(1-x^2)\,\Gamma_d'' = p_2\,\Gamma_d - 2mxy_d/(1-x^2) - mu_n + mq_n, \qquad (14c)$$

$$(1-x^2)\,q_n' = p_2\,y_d + m\Gamma_d', \qquad (14d)$$

whose coefficients $p_2 = p_1+\frac{1}{4}-\bar{\alpha}^2$, $p_3 = p_1-2\bar{\alpha}^2-\frac{3}{2}$, and $p_4 = \bar{\alpha}^2-\frac{9}{4}$ are even functions of $\bar{\alpha} = \alpha-\frac{1}{2}$. This renders obvious the fact that the eigenvalue spectrum is symmetric

with respect to line $\alpha = \frac{1}{2}$ on the complex plane (α_r, α_i), if boundary conditions for disturbances are also even functions of $\bar{\alpha}$. Below, we show analytical solutions of (14) for different boundary conditions that will be used as starting and checking points for the numerical calculations that follow.

3.2. *Spectrum for the unbounded still fluid*

First, consider the case when the fluid occupies the entire space, i.e. $x_c = -1$ and $-1 \leqslant x \leqslant 1$. The requirement of velocity boundedness on the axis, $x = \pm 1$, yields

$$y_d(\pm 1) = \Gamma_d(\pm 1) = 0. \tag{15}$$

For u_n and q_n, (7*c*) transforms to

$$\left.\begin{aligned} &u_n(\pm 1) = 0 \quad \text{for} \quad m \neq 0 \\ &\pm 2u_n'(\pm 1) = [2(\alpha - \tfrac{1}{2})^2 + \tfrac{3}{2}]\, u_n(\pm 1) - p_4\, q_d(\pm 1) \quad \text{at} \quad m = 0, \end{aligned}\right\} \tag{16}$$

and, therefore, the spectrum is symmetric with respect to the line $\alpha = \frac{1}{2}$.

The eigenvalues α of (14)–(16) are integers and the eigenfunctions are (Legendre) polynomials (Happel & Brenner 1986, §3-2). Some of the eigenvalues corresponding to conservation laws are common for $Re \neq 0$ as well. Also, the multiplicity of eigenvalues at $Re = 0$ must be taken into account for calculations of α in the vicinity of $Re \neq 0$. Now we briefly review the features of the $Re = 0$ spectrum which are important for the stability study of conical flows in §§4–6.

3.2.1. *Disturbances of swirl*

In the simplest case, $m = 0$, the meridional motion and swirl are uncoupled. For swirl modes, $\Gamma = r^{\alpha}\Gamma_d(x)$, one can use $y_d = u_d = q_d \equiv 0$, and (14*c*) becomes

$$(1 - x^2)\,\Gamma_d'' = (\alpha - \alpha^2)\,\Gamma_d. \tag{17}$$

We denote eigenvalues as $\alpha_{mn}^{\pm}$, where $\pm$ indicates sign of α, m is the azimuthal wavenumber and n denotes the number of the $\Gamma_d(x) = 0$ roots in $-1 < x < 1$. Eigenvalues of (17) with condition (15) are integers, given by

$$\alpha_{0n}^{+} = n + 2, \quad \alpha_{0n}^{-} = n - 1 \quad \text{with} \quad n = 0, 1, 2, \ldots, \tag{18}$$

Both α_{0n}^{+} and α_{0n}^{-} correspond to the eigenfunction

$$\Gamma_d = (1 - x^2)\,P_n(x), \tag{19}$$

where $P_n(x)$ is a (even and odd) polynomial of power n (for even and odd n). For fixed n, the positive and negative eigenvalues (18) correspond to the same eigenfunction, because the value of $\alpha - \alpha^2$ $(= \frac{1}{4} - (\alpha - \frac{1}{2})^2)$ in (17) is the same.

The case $n = 0$ is of special interest, since this solution explicitly follows from the conservation of angular momentum. Indeed, the eigenfunction $\Gamma_d = C(1 - x^2)$ describes solid-body-type distribution of swirl on a spherical surface $r = r_0$, while $\alpha_{00}^{+} = 2$ $(\Gamma = Cr^2 \sin^2\theta)$ corresponds to solid-body-type rotation inside the sphere $r < r_0$. For this solution, the angular momentum flux through $r = \text{const} \leqslant r_0$ is zero. The eigenvalue $\alpha_{00}^{-} = -1$ $(\Gamma = Cr^{-1}\sin^2\theta)$ corresponds to the distribution of swirl for $r > r_0$, with the angular momentum flux $(\sim r^2 \partial\Gamma/\partial r)$ through any surface surrounding the sphere remaining constant. Conservation of angular momentum implies that the eigenvalues, $\alpha = 2$ and $\alpha = -1$, (but not their eigenfunctions!) are the same for all x_c. Numerical calculations agree with this feature (see §3.3 and figure 3).

3.2.2. *Disturbances of the meridional motion*

One can use $\Gamma_d \equiv 0$ and introduce the stream function: $u_d = -\psi'$, $y_d = -(1+\alpha)\psi$. Then (14) reduces to

$$(1-x^2)\psi'''' - 4x\psi''' = p[2\psi'' - (2+p)\psi/(1-x^2)], \quad p = \alpha(1-\alpha). \tag{20}$$

One special solution demands our attention: $\psi = C(1-x^2)$ at $\alpha = 0$ and $\alpha = 1$. There are no such eigenvalues for swirl modes; moreover, these eigenvalues are simple (in contrast to others which are triple). It is easily shown that $\alpha = 1$ corresponds to a uniform flow directed along the symmetry axis. The case $\alpha = 0$ corresponds to a flow induced by a point source of the axial momentum, i.e. Landau's jet for $Re \gg 1$. If the axial momentum flux is fixed (a natural requirement for an entire-space problem), then the disturbance with $\alpha = 0$ is not allowed. Therefore, neither of these cases is relevant for our study.

Another special eigenvalue is $\alpha_{00}^- = -1$, where $y_d \equiv 0$, i.e. (15) is satisfied automatically. There are three eigenfunctions at $\alpha_{00}^- = -1$: (i) $u_d = \text{const}$, $q_d = 0$, corresponding to a flow induced by a point source of fluid, (ii) $\psi = Cx(1-x^2)$, corresponding to a dipole source of the axial momentum, and (iii) $\psi \equiv 0$, $\Gamma_d = 1-x^2$, described in §3.2.1. According to the symmetry of spectrum, $\alpha_{00}^+ = 2$ is also a triple eigenvalue. When we consider the other special solution, (13*a*), it becomes evident, owing to physical meaning (angular momentum conservation and uniform pressure), that the eigenvalues, $\alpha_{00}^- = -1$ and $\alpha_{00}^+ = 2$, exist for arbitrary basic flows.

3.2.3. *Azimuthal disturbances*

The eigenvalues for $m \geqslant 1$ are also integers as are those for $m = 0$. In particular, $\alpha_{m0}^- = 1-m$ and $\alpha_{m0}^+ = m$ with the eigenfunctions:

$$\left.\begin{aligned} &u_n = (1-x^2)^{m/2}, \quad y_d = x(1-x^2)^{m/2}/(m+1), \quad \Gamma_d = (1-x^2)^{m/2}/(m+1), \\ &q_n = (1-x^2)^{m/2}(m-1)/(m+1). \end{aligned}\right\} \tag{21}$$

Here the integration constant is chosen via the normalization, $u_n(0) = 1$. There are also eigenvalues, $\alpha_{mn}^- = 1-m-n$ and $\alpha_{mn}^+ = m+n$, $n = 1, 2, \ldots$, whose eigenfunctions are those in (21) multiplied by a polynomial of power n. Some of the solutions (21) have simple physical meanings. In particular, consider $m = 1$ when the solutions are:

$$\left.\begin{aligned} &\{\alpha_{10}- = 0, \quad u_d = q_d = 2\Gamma_d = (1-x^2)^{1/2}, \quad y_d = \tfrac{1}{2}x(1-x^2)^{1/2}\}, \\ &\{\alpha_{10}+ = 1, \quad u_d = \Gamma_d = (1-x^2)^{1/2}, \quad y_d = x(1-x^2)^{1/2}, \quad q_d = 0\}. \end{aligned}\right\} \tag{22}$$

The 'neutral disturbance' with $\alpha_{10}^- = 0$ is similar to that with $\alpha = 0$ in §3.2.2, but now the jet axis is positioned on the equatorial plane. The mode with $\alpha = 1$ corresponds to a uniform flow directed along a normal to the z-axis. Solutions (22) exist also for some basic flows but are not related to any instability or bifurcation.

3.3. *Spectrum for a conical region*

For the problem in the half-space, $0 \leqslant x \leqslant 1$, with the symmetry (i.e. stress-free) condition, $\psi = \psi'' = \Gamma_d' = 0$ at $x = x_c = 0$, the solutions are the same as those for the whole space but only with even n in (18). For the no-slip condition, $\psi(0) = \psi'(0) = \Gamma_d(0) = 0$, the solutions for swirl are again the same as those for the whole space but this time only with odd n. The solutions for meridional motion correspond to all $n \geqslant 2$ but now there is just one eigenfunction for each eigenvalue. For a flow in the region, $x_c \leqslant x \leqslant 1$, $x_c \neq -1$ and 0, we find α numerically. Since the triple spectrum (at $x_c = -1$) is degenerate, a change in x_c, like any other modification of the problem, transforms α into three (real or complex-conjugate) eigenvalues.

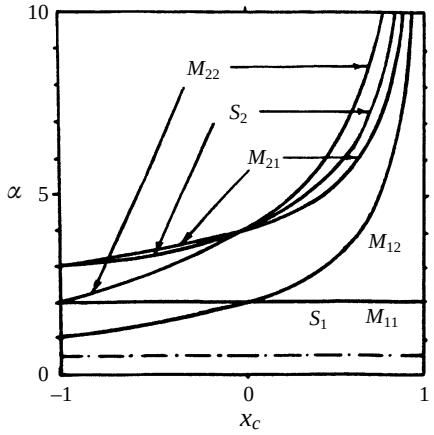

FIGURE 3. The eigenvalues α versus cone angle θ_c ($x_c = \cos\theta_c$) for axisymmetric disturbances satisfying the stress-free conditions at $x = x_c$. M and S denote the meridional and swirl modes. The spectrum is symmetric with respect to the chain line ($\alpha = 0.5$). Figures 3–4 depict a still fluid inside the $x = x_c$ cone.

3.3.1. *Shear-stress-free condition*

First, we apply a special problem modification (unfolding) considering $x = x_c$ as the impermeable and stress-free boundary:

$$\psi(x_c) = 0, \quad \psi''(x_c) = 0, \quad (1-x_c^2)\,\Gamma_d'(x_c) + 2x_c\,\Gamma_d(x_c) = 0, \tag{23}$$

and conditions (15)–(16) at $x = 1$. These results will be useful in the later stability analysis (§5). We apply the following numerical procedure. For the swirl modes, we integrate (17) from $x = x_c$ with the initial conditions (23) and normalization $\Gamma_d(x_c) = 1$. Since $x = 1$ is a singular point, we integrate (17) to $x = x_f = 0.9999$ and apply the extrapolation, $\Gamma_d(1) = \Gamma_d(x_f) + (1-x_f)\,\Gamma_d'(x_f)$. Now we consider this quantity $\Gamma_d(1)$ as a function of α, and look for its zeros. To find these zeros numerically we apply the Newton shooting procedure, using the previous solution as an initial guess, and starting from the known analytical solutions. The analogous algorithm is used for the calculation of meridional modes but in this case the shooting is multidimensional. Figure 3 shows the dependence of a few eigenvalues on the cone angle; here M indicates the eigenvalue relating to disturbances of the meridional motion, while S denotes that relating to swirl. The first index can be any integer and labels eigenvalues of the swirl modes as α increases; the second index equals 1 or 2 and denotes the corresponding two modes of the meridional motion. Value 1 of the second index corresponds to the smaller power of a polynomial for $\psi(x)$. This numeration of the modes is made at $x_c = 0$. The triple eigenvalue, $\alpha = 4$ at $x_c = 0$, splits into three simple eigenvalues (S_2, M_{21},M_{22}) for $x_c \neq 0$. The triple eigenvalue, $\alpha = 2$ (at $x_c = 0$) splits into one simple (M_{12}) and one double (S_1, M_{11}) eigenvalue, the letter being the same for all x_c. The double eigenvalue occurs because both the rigid-body rotation (mode S_1) and the uniform change of pressure (mode M_{11}) satisfy all the boundary conditions. For negative α one must recognize that the curves in figure 3 are symmetric with respect to the chain line, $\alpha = \frac{1}{2}$.

3.3.2. *Unfolding under the condition of zero flow force*

In some basic flows, the flow force is given and fixed (§5) and, therefore, must fulfil (12). Since only three conditions can be set at $x = x_c$, (12) must replace one of the

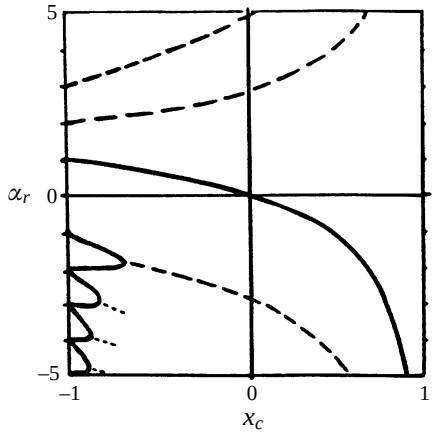

FIGURE 4. The real part of α for flow-force-free disturbances of the meridional motion: ——, real α; – – –, complex α (also in the following figures).

conditions given in (23). As the surface is impermeable and stress-free with respect to swirl, it is reasonable to replace $\psi''(x_c) = 0$ by (12), both being conditions for the meridional flow. For the still fluid, (12) reduces to

$$J_d = \{xq_d - 2x(1-\alpha)\psi' - (\alpha-2)\psi + (1-x^2)\psi''\}\,\mathrm{d}x = 0, \tag{24}$$

where $q_d = (1+\alpha)[2x\psi'' - 2(\alpha^2-\alpha+1)\psi' - (1-x^2)\psi''']/[(\alpha-\frac{1}{2})^2 - \frac{9}{4}] - \psi'$ from (14*b*). Condition (24) decreases the degeneracy of the spectrum and also breaks the symmetry with respect to $\alpha = \frac{1}{2}$.

When we examine the whole space ($x_c = -1$), we find that all the swirl modes of §3.2.1 satisfy (24), since $u_d = y_d = q_d \equiv 0$. Similarly, the meridional modes of §3.2.2, where ψ is an odd polynomial of x, are all valid as (24) is satisfied automatically. For even polynomials of x, (24) excludes the mode, $\psi = C(1-x^2)$, at $\alpha = 0$ ('Landau jet') but not at $\alpha = 1$ (Gallilean transformation). It appears that other even polynomials satisfy (24), so that eigenvalues are triple at $x_c = -1$. For $x_c \neq -1$, the eigenvalues become simple, but different to that specified in §3.3.1.

Figure 4 shows the spectrum for a few meridional modes (the spectrum for swirl modes is simple and is not shown). The solid curves correspond to real α and the dashed curves show α_r for complex α. The double eigenvalues $\alpha = 2$ and 3 at $x_c = -1$ become complex for $x_c > -1$. First, the double eigenvalues $\alpha = -2, -3, \ldots$, at $x_c = -1$ split into two separate real values as x_c increases. Then the real eigenvalues merge again, but form other pairs. For example, the solid curves, which start at $\alpha = -1$ and -2, merge, followed by a dashed curve. Similar dashed curves, located below, have not been calculated and indicate only the trends.

Note that the eigenvalue originating from $\alpha = 1$ at $x_c = -1$ remains real for all x_c. One can see that the corresponding curve in figure 5 intersects the line, $\alpha = 0$, at $x_c = 0$. This 'instability' of the still fluid corresponds to a specific feature of the Squire jet at $x_c = 0$, namely, the existence of two solutions at any given $J_1 > 0$ and the absence of any solution at $J_1 < 0$ (see §4).

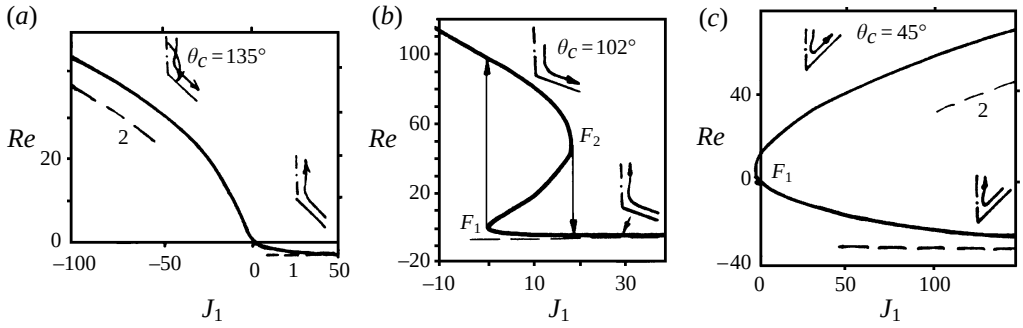

FIGURE 5. Non-uniqueness of the Squire solutions. Relations between the flow force J_1 and the surface velocity Re at (*a*) $x_c = -0.707$; (*b*) -0.2; (*c*) 0.707. ——, Numerical results; – – –, asymptotes. Insets show flow patterns for $Re > 0$ (the upper insets) and $Re < 0$ (the lower ones).

4. Axisymmetric instability of swirl-free jets

4.1. *Swirl-free jet*

When swirl Γ and body force f_b are absent, (4*b*) and (7*a*) yield $F = C(1-x)^2$. Then the analytical solution of (4*a*) is (Yatseev 1950; Squire 1952):

$$\psi = 2\alpha(1-x)[(1+x)^n-(1+x_c)^n]/[\alpha-(1+x)^n] \quad \text{for} \quad C < \tfrac{1}{2}, \tag{25a}$$

$$\psi = (1-x)/\{2/\ln[(1+x)/(1+x_c)]-1\} \quad \text{for} \quad C = \tfrac{1}{2}, \tag{25b}$$

$$\psi = 2C(1-x)/\{\omega\cot(\tfrac{1}{2}\omega\ln[(1+x)/(1+x_c)])-1\} \quad \text{for} \quad C > \tfrac{1}{2}. \tag{25c}$$

Here $\alpha = (1+n)/2$, $\alpha = (1+x_c)^n(1+n)/(1-n)$, $\omega = \mathrm{i}n$, $n = (1-2C)^{1/2}$; and

$$Re = -C(1-x_c)/(1+x_c), \tag{26}$$

where Reynolds number $Re = rv_{rc}/\nu = -\psi'(x_c)$ is based on the radial velocity at the surface, $x = x_c$.

Features and applications of solution (25) depend on what serves as a control parameter. If Re is the control parameter, then no regular solution exists for large negative Re (negative Re corresponds to a flow converging to the symmetry axis along the surface $x = x_c$). The regular solution ceases to exist (i.e. 'collapse' occurs) at $Re = Re_{co}$ owing to the appearance of a singularity on the axis (Bratukhin & Maurin 1967). As $Re \to Re_{co}$, a strong near-axis jet develops, whose axial velocity becomes infinite at $Re = Re_{co}$. It thus seems paradoxical that a singularity occurs in a viscous solution at a finite Re.

This paradox is absent in the problem where the flow force J_1 (§2.4.4) is the control parameter. The solution is regular for any J_1, and as $J_1 \to \infty$, Re has a bounded limiting value, e.g. $Re = -2$ at $x_c = -1$. However, there are other intriguing features, such as solution non-uniqueness and hysteretic transitions.

4.2. *Hysteresis*

4.2.1. *Solution non-uniqueness*

The solution is unique for the Landau jet ($x_c = -1$): each value of J_1 corresponds to just one solution. This is also valid for flows above cones with angles in the range $\theta_K \leqslant \theta_c \leqslant 180°$ (θ_K corresponds to a cusp catastrophe, see §4.2.2). Figure 5(*a*) shows $Re(J_1)$ at $x_c = -0.707$ ($\theta_c = 135°$). The flow force J_1 varies from $-\infty$ to $+\infty$, but Re is bounded from below. As $J_1 \to \infty$, Re approaches the asymptotic value -3.3

(dashed line 1) which corresponds to the collapse (§4.1) when Re is a control parameter. As $J_1 \to -\infty$, Re approaches the asymptote (Shtern & Hussain 1996),

$$J_1 = \tfrac{1}{3} x_c (1-x_c^2)^{1/2} (2Re)^{3/2}, \tag{27}$$

(curve 2). The insets in figure 5(*a*) show the descending ($J_1 < 0$) and ascending ($J_1 > 0$) flow patterns.

As x_c increases, relation $Re(J_1)$ qualitatively changes. Figure 5(*b*) shows $Re(J_1)$ at $x_c = -0.2$ ($\theta_c = 102°$). The range of Re is again bounded from below by asymptote $Re = -5.9$ (dashed line), but function $Re(J_1)$ is no longer single-valued: the corresponding (solid) curve has folds F_1 and F_2. There are three different Re for each J_1 in the range $J_{1\,min} = -0.0094 < J_1 < 18.5 = J_{1\,max}$. In particular, there are three solutions with zero flow force: the still fluid ($Re = 0$), and two descending flows with $Re = 0.49$ and $Re = 98$.

As one moves along the upper branch with increasing J_1, it is impossible to avoid a jump transition to the lower branch at F_2 (shown by an arrow in figure 5*b*). This transition transforms the flow pattern from that shown in the upper inset of the figure to that shown in the lower inset. Thus, it corresponds to a jump separation of the outflow from the cone surface. Similarly, as one moves along the lower branch with J_1 decreasing, an opposite transition is unavoidable at F_1 (shown by an arrow in figure 5*b*): a jump attachment of the outflow to the cone surface. Hence, the intriguing features mentioned above: solution non-uniqueness and hysteretic transitions.

There is another qualitative change in relation $Re(J_1)$ as x_c increases even further. The two-branch solid curve in figure 5(*c*) shows $Re(J_1)$ at $x_c = 0.707$ ($\theta_c = 45°$). As $J_1 \to \infty$, the lower branch approaches the asymptote, $Re = -31$ (dashed line 1) and the upper branch approaches asymptote (27) shown by curve 2. The branches meet at fold F_1 ($J_1 = J_{1\,min} = -3.4$, $Re = 7.2$); fold F_2 of figure 5(*b*) disappears in figure 5(*c*). There are two solutions for each $J_1 > J_{1\,min}$ and no solutions for $J_1 < J_{1\,min}$. To see how the number of solutions varies as x_c increases, we draw a catastrophe map.

4.2.2. *Catastrophe map*

Fold points F_1 and F_2 (such as those in figure 5*b*, *c*) projected in the control parameter plane (J_1, x_c) form curves F_1 and F_2 shown in figure 6. Note that the efficient presentation of the results requires a logarithmic scale for $J_1 > 0.1$, with a linear scale for $J_1 < 0.1$. As x_c decreases, curves F_1 and F_2 meet, terminating at the cusp point K ($J_1 = J_K = -0.35$, $x_c = x_K = -0.447$, $\theta_K = 117°$). This means that there exists a unique solution at any value of J_1 for $x_c < x_K$ (for $x_c = -0.707$ see figure 5*a*). On curve F_1 in figure 6, $J_{1\,min}$ is negative at any x_c except at $x_c = 0$ where curve F_1 is tangential to the line, $J_1 = 0$. This also follows from analytical calculations using the Taylor expansion for a solution near $Re = 0$. According to (25), $\psi = Re(x_c - x)(1-x)/(1-x_c) + O(Re^2)$, and calculations give $J_1 = -2Rex_c^2 + O(Re^2)$. Therefore, J_1 is negative for small positive Re independent of the x_c sign; it follows that $J_{1\,min}$ must be negative as well. The case $x_c = 0$ is exceptional: $J_1 \geqslant 0$ with $J_1 = J_{1\,min} = 0$ at $Re = 0$.

Along curve F_2 in figure 6, J_1 increases with x_c and tends to infinity as $x_c \to 0$. Also Re corresponding to fold F_2 (e.g. see figure 5*b*) tends to infinity. A strong jet develops near the surface, and flow becomes irrotational outside this boundary layer. It follows from (25) that this outer solution is

$$\psi_p = \psi_c (1-x)/(1-x_c), \quad \psi_c = [2Re(1-x_c^2)]^{1/2},$$

(subscript p denotes potential solution and c denotes values on the cone surface $x = x_c$) which gives the contribution to the flow force as

$$J_p = \psi_c^2 \ln 2. \tag{28}$$

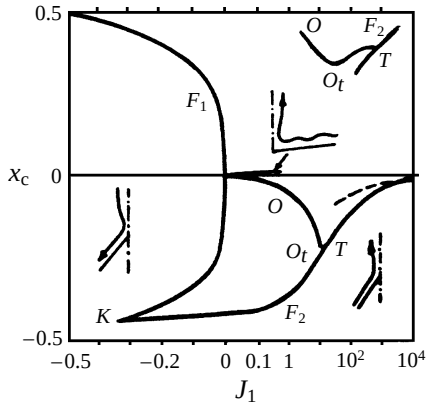

FIGURE 6. Catastrophe map for the Squire solutions. Folds F_1 and F_2 meet and terminate at cusp K. The dashed curve is the asymptote for F_2. For $x_c < 0$, there are three solutions in the region between F_1 and F_2 and a unique solution outside. For $x_c > 0$, there are two solutions to the right and no solution to the left of F_1. Curve O is neutral for oscillatory disturbances. The insets are sketches of the primary (below) and secondary (above) flows; also the enlarged vicinity of triple point T is shown in the upper right-hand corner.

The first two terms of the boundary-layer expansion are

$$\psi_b = -\psi_c V_1(\xi) + V_0(\xi) + \dots,$$
$$u = -\psi' = Re\, U_2(\xi) - \psi_c U_1(\xi) + \dots, \quad \xi = \tfrac{1}{2}(x - x_c)\psi_c/(1-x_c^2),$$
$$V_1 = \tanh\xi, \quad V_0 = 2(1+x_c)\xi\tanh\xi - (1-x_c)(\tanh^2\xi - \xi^2\cosh^{-2}\xi),$$
$$U_2(\xi) = \cosh^{-2}\xi,$$
$$U_1 = (\tanh\xi + \xi\cosh^{-2}\xi)/(1-x_c) - [(1+\xi^2)\tanh\xi - \xi](1+x_c)^{-1}\cosh^{-2}\xi.$$

Taking only terms of $O(\psi_c^2)$ and larger ones into account in (11), we obtain,

$$j_b = \tfrac{1}{4}x_c\psi_c^4 U_2^2 + \tfrac{1}{2}\psi_c^3\xi U_2^2 - \tfrac{1}{2}(\psi_b^2)'. \tag{29}$$

We use $x_c = 0$ (in (29) except for the first term. Integrating the last term of (29) across the boundary layer yields $-\frac{1}{2}\psi_c^2$. The integral of U_2^2 is also found analytically as $4/(3\psi_c)$, whereas numerical integration of ξU_2^2 gives d/ψ_c with $d = 0.2954$. We then add the jet flow force and J_p obtained in (28) above, yielding

$$J_1 = d_1\psi_c^2 + \tfrac{1}{3}x_c\psi_c^3, \quad \text{where} \quad d_1 = d - \tfrac{1}{2} + \ln 2.$$

Since $d_1 = 0.489$ and $x_c < 0$, the asymptotic relations for fold F_2 as $x_c \to 0$ are:

$$Re = 2d_1^2/x_c^2, \quad J_{1\,max} = 4d_1^3/(3x_c^2) = 0.155/x_c^2.$$

The latter relation is shown by the dashed curve in figure 6.

Thus, the number of solutions (in the region of non-uniqueness) changes from three to two as x_c increases and passes zero, because both fold F_2 and the upper branch (see figure 5*b*) go to infinity. The general theory (Iooss & Joseph 1981) claims that only one branch of a fold can correspond to stable solutions. Therefore, at least one branch of the solid curve in figure 5(*c*) corresponds to unstable solutions. Similarly, the intermediate branch, connecting folds F_1 and F_2 in figure 5(*b*), seems to correspond to unstable solutions. To clarify which branches are unstable and what disturbances grow from them we study the stability of the above solutions.

4.3. *Fold-catastrophe instability*

4.3.1. *Stability equations for meridional motion*

Since the folds and hysteretic transitions occur here in swirl-free flows, the study of their stability can be restricted to disturbances of the meridional motion only. At $m = 0$ and $\Gamma_b = 0$, (6) yields the decoupled system for the meridional disturbances:

$$y_d' = (1+\alpha)\, u_d, \tag{30a}$$

$$(1-x^2)\, u_d'' = (2x-y_b)\, u_d' + [(\alpha-2)\, u_b - \alpha - \alpha^2]\, u_d - u_b'\, y_d + (\alpha-2)\, q_d - 2y_b\, y_d/(1-x^2), \tag{30b}$$

$$(1-x^2)\, q_d' = (1-x^2)\,(1-\alpha)\, u_d' + [\alpha - \alpha^2 - (1-\alpha)\, u_b]\, y_d - (1+\alpha)\, y_b\, u_d - 2xy_b\, y_d/(1-x^2), \tag{30c}$$

The numerical algorithm is similar to that for the still fluid (see §§3.3.1) and $y_b = -\psi$, $u_b = -\psi'$ with ψ taken from (25). The folds (figure 6) for the basic solutions must be the neutral curves ($\alpha_r = 0$) for disturbances. This requirement and the analytical results obtained for the fluid at rest serve as a check for the numerical calculations that follow. First, however, we find one more analytical solution studying (30).

4.3.2. *Analytical solution*

As figure 6 shows, curve F_1 passes through the joint $J_1 = x_c = 0$, where the primary flow vanishes and hence we again have the still fluid case. The fold at $J_1 = x_c = 0$ corresponds to the crossing line $\alpha_r = 0$ by the solid curve in figure 4. The analytical solution for this point is

$$\alpha = 0, \quad y_d = x(1-x), \quad u_d = 1-2x, \quad q_d = -2x, \quad \Gamma_d \equiv 0, \tag{31}$$

where the normalization, $u_d(0) = 1$, is applied. It can be seen that solution (31) is regular on the axis ($x = 1$) and that it satisfies both (30) and the impermeability condition, $y_d(0) = 0$. We must determine whether this disturbance is flow-force free. Substituting (31) into (12) (see also (24)) yields the flow force density

$$j_d = 2(1-3x^2). \tag{32}$$

Integrating (32) from $x = 0$ to $x = 1$ yields $J_d = 0$ and thus confirms that the neutral disturbance (31) is indeed flow-force free.

Starting from the analytical solution (31) at $x_c = 0$, we numerically calculate α near the folds and find that α is real, and the $\alpha = 0$ curve coincides with the folds F_1 and F_2 in figure 6, thus confirming conclusions so far. Now we study the origin of the neutral disturbances.

4.3.3. *Instability near the cusp point*

We start from the case $x_c = -0.5$, which corresponds to a horizontal line positioned below the cusp K in figure 6. At this x_c, the primary solution is unique for any given J_1.

Figure 7(*a*) shows the dependence of $Re_a = rv_a/\nu, v_a$ is a velocity on the axis, on J_1 (curve J_1) and α (curve α) for the 'most dangerous' disturbance mode (obtained by numerical calculations of the problem for the basic flow and disturbances). Note that $\alpha > 0$ at $Re_a = J_1 = 0$ (i.e. for the still fluid), so that this mode corresponds to outer disturbances. It can be seen that α decreases as it approaches the inflection point of curve $Re_a(J_1)$. Although minimal in the vicinity of the inflection point, α does not change its sign when $Re_a(J_1)$ is a single-valued function (hence no instability).

Figure 7(*b*) shows similar data but for $x_c = -0.44$ which corresponds to a horizontal

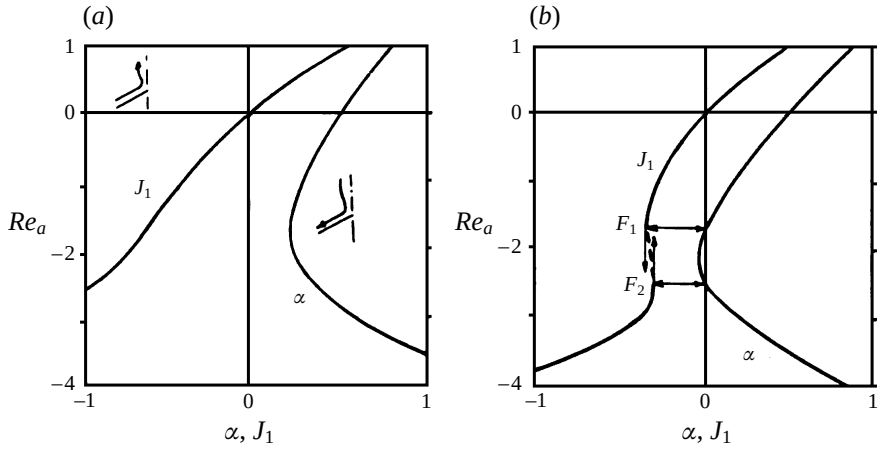

FIGURE 7. Relations between flow force J_1, axial velocity Re_a, and eigenvalue α at (*a*) $x_c = -0.5$, (*b*) -0.44. The horizontal arrows in (*b*) show that the extrema of J_1 and the zeros of α are at the same Re_a. The vertical arrows show jump transitions between the regimes.

line positioned slightly above the cusp level, $x_c = x_K = -0.447$, in figure 6. Now $Re_a(J_1)$ (curve J_1 in figure 7*b*) is a three-valued function in a thin region near the inflection point. The horizontal arrows in figure 7(*b*) show that the sign of α changes at folds F_1 and F_2 (corresponding to the minimum and maximum of J_1). As curve α in figure 7(*b*) shows, $\alpha > 0$ for the upper and lower branches of curve J_1, which means that the corresponding outer disturbance decays as r decreases. The value of α (i.e. the decay rate) decreases as one approaches fold F_1 along the upper branch of curve J_1. The α value becomes negative on the middle branch of curve J_1, which means that the disturbance, given at the outer boundary of the similarity region, now increases as r decreases. Therefore, the corresponding solution is unstable, and, to denote this, the broken line represents the middle branch of curve J_1. The vertical arrows in figure 7(*b*) show the jump transitions occurring when J_1 increases (the right-hand arrow) and decreases (the left-hand arrow) while passing through the fold points.

Thus, we verify that folds F_1 and F_2 in figure 6 are neutral curves. The fold bifurcations and jump switching between the steady regimes are caused by outer disturbances for $x_c < 0$, and the solutions corresponding to the middle branch of the hysteresis loop are unstable with respect to these disturbances.

4.3.4. *Reconnection of spectral branches and genesis of global modes*

As x_c increases from x_K, significant metamorphoses of the eigenvalue spectrum occur, leading to a new type of instability (to be described in §4.4). Figure 8(*a*) shows curve $Re_a(J_1)$ for the basic solution, while figure 8(*b*) shows how eigenvalues vary with Re at $x_c = -0.34$. The solid curves show real α, the dashed curves show α_r for complex α, and the chain curves show α_i along path $CM_1M_2M_3F_2$. At $Re = 0$, eigenvalues $\alpha = 0.375$ (point R) and $\alpha = -2.32 \pm i0.502$ (point C) coincide with those found for the still fluid (the solid and lower dashed curves in figure 4 at $x_c = -0.34$).

As Re decreases along CM_1, the complex-conjugate eigenvalues approach each other and merge at point M_1 in figure 8(*b*). For smaller Re, these eigenvalues become real. One of the new real α (branch M_1M_2) approaches the larger real α (branch RM_2), coinciding with it at point M_2; they then become complex-conjugate for smaller Re (path M_2M_3). As Re further decreases, these eigenvalues become real again at point M_3. Compare path $RM_2M_3F_2$ in figure 8(*b*) with curve α in figure 7(*b*). Note that, as

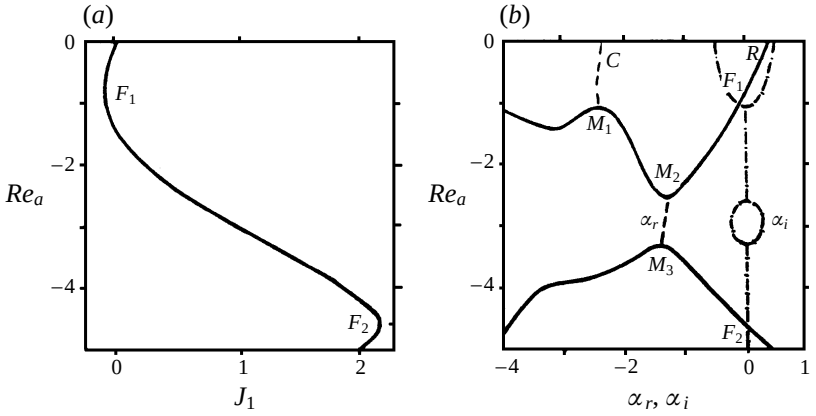

FIGURE 8. (*a*) The intermediate branch of the basic solutions and (*b*) the disturbance spectrum at $x_c = -0.34$. (*b*) ——, real α; – – –, real part α_r; –·–, imaginary part α_i (along path $CM_1M_2M_3F_2$) of complex α.

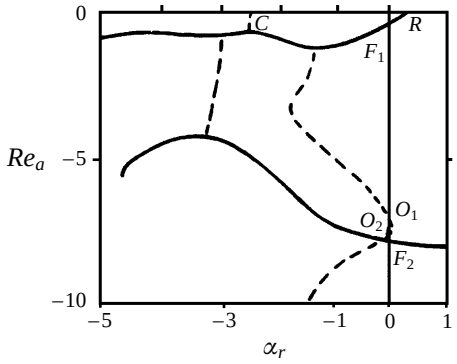

FIGURE 9. The real part of α for the intermediate branch at $x_c = -0.227$. Intersections of the dashed curve with line $\alpha_r = 0$ are the neutral points, O_1 and O_2, for the oscillatory instability.

x_c decreases, points M_2 and M_3 become closer, then merge, and reconnection of the real branches occurs, so that path $RM_2M_3F_2$ in figure 8(*b*) becomes curve α in figure 7(*b*).

The physical interpretation of this reconnection is as follows. Since $\alpha > 0$ at $Re = 0$ for path RM_2 in figure 8(*b*), this spectral branch corresponds to the outer disturbances. On the other hand, since $\alpha_r < 0$ at $Re = 0$ for path CM_1M_2, this spectral branch corresponds to the inner disturbances. As a result of the merging of these branches at M_2, the disturbances become both inner and outer. This joint influence of conditions at both the boundaries, $r = r_i$ and $r = r_o$, makes the disturbances global. The global modes oscillate in the radial direction since α is complex along M_2M_3 in figure 8(*b*). For larger x_c, these oscillating disturbances becomes neutral, i.e. $\alpha_r = 0$, as shown below.

4.4. *Oscillatory instability*

4.4.1. *Appearance of space-oscillatory instability*

As x_c increases further, the dashed curve M_2M_3 shown in figure 8(*b*) extends and bends, resulting in the appearance of local minima and maxima of α_r. The maximum approaches, touches, and intersects the line $\alpha_r = 0$. Figure 9 shows the spectrum pattern at $x_c = -0.227$. This is slightly larger than the value of x_c corresponding to the tangency of the right-hand dashed curve with line $\alpha_r = 0$. The intersection points O_1

and O_2 of this curve with line $\alpha_r = 0$ corresponds to neutral disturbances. This intersection indicates bifurcation of the secondary steady solutions periodic with respect to $\xi = \ln(r/r_0)$. The velocity ratio of the amplitude of these oscillations and the primary flow does not depend on r. The wavelength in ξ is $2\pi/|\alpha_i|$ ($\alpha_i = \pm 3.25$ when curve α_r touches line $\alpha_r = 0$).

The oscillatory solution seems to contradict dimensional analysis. To make the logarithm argument dimensionless, one needs some lengthscale r_0, i.e. to use $\ln(r/r_0)$. However, the problem has no intrinsic lengthscale. One cannot deduce a lengthscale from the given quantities (ρ, ν, and J having the same dimension as $\rho\nu^2$). Nevertheless, the oscillating solution obtained depends on some (not given) r_0.

An analogous phenomenon occurs in the planar vortex-source flow (Goldshtik, Hussain & Shtern 1991). The given characteristics are only flow rate Q, circulation Γ_d, and ν, all having the same dimension. However, an arbitrary scale r_0 appears in the secondary spiral flows which depend on $\chi = \phi - \beta \ln(r \sin\phi/r_0)$. A change in r_0 merely causes a turn of the secondary flow around the origin. Since there is no preferable azimuthal angle ϕ in the problem formulation, any shift in ϕ is admissible and this corresponds to the freedom in the choice of r_0. This role of r_0 in the planar vortex-source is less significant than that in the case considered here.

In the present paper, a change in r_0 causes a phase shift of the oscillating solution in the radial direction. This appears to be a more radical modification of the flow than the turn around. The phase shift in practical flows can be specified by conditions outside the similarity region. As one moves in toward the similarity region, the flow 'remembers' the phase as well as conservative quantities (such as the flow force J). It is typical that the phase is a free parameter of periodic solutions (e.g. for Taylor's vortices and thermal-convection rolls), and that the phase is specified by boundary conditions in practical confined flows.

The physical significance of the oscillatory solutions is questionable if they bifurcate only from the unstable primary solution and are therefore also unstable. One can see this in figure 9: points O_1 and O_2 are within the interval bounded by the fold points F_1 and F_2; this interval corresponds to unstable primary solutions. If the control parameters are altered, can bifurcation of the oscillatory solution from the stable primary solution then occur? To answer this question, we must obtain a neutral curve characterizing the oscillatory instability in the parameter plane (J_1, x_c).

4.4.2. *Neutral curve*

We start from the data for points O_1 and O_2, gradually vary one of the parameters J_1 and x_c, and adjust the other so as to satisfy $\alpha_r = 0$. (This gradual variation is required for the convergence of the Newton shooting procedure applied for this numerical adjustment.) Curve O in figure 6 shows the neutral curve for the oscillatory instability. The minimum point O_t of this curve corresponds to the tangency discussed above. This point is inside the region bounded by curves F_1 and F_2 (§4.4.1). It is so close to curve F_2 that the accuracy of the drawing of the main plot in figure 6 does not allow distinction of O_t from F_2; the inset in the right-hand upper corner shows the enlarged vicinity of O_t.

As x_c increases along the left branch of curve O in figure 6, $|\alpha_i|$ also increases. This branch passes through the point ($J_1 = 0$, $x_c = 0$) corresponding to the still fluid in the half space. This reveals one more spectral branch for the still fluid shown by the bold vertical line, $x_c = 0$, in figure 4. It is striking that this branch exists only at $x_c = 0$. The intersection of this vertical line and the solid curve in figure 4 is not to be viewed as spectrum degeneracy, since $|\alpha_i| \neq 0$ on the vertical line at the intersection point. So

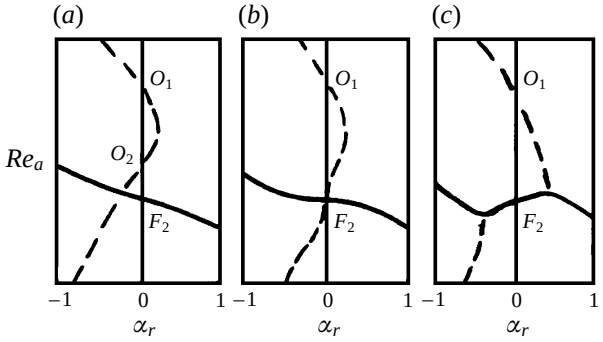

FIGURE 10. A spectrum transformation near the triple point T in figure 6. Arrangement of the neutral points for the oscillatory, O_1 and O_2, and fold. F_2, bifurcations at (*a*) $x_c < x_{cT}$, (*b*) $x_c = x_{cT}$, and (*c*) $x_c > x_{cT}$.

there are the eigenvalues, $\alpha = 0$ and $\alpha = \pm \mathrm{i}\, 7.86$, corresponding to the neutral disturbances at $x_c = 0$. Since the centre manifold (subspace of neutral disturbances) is three-dimensional, a complex (possibly chaotic) flow state can exist in the vicinity of the point ($J_1 = 0$, $x_c = 0$) in figure 6. To clarify this, one would need a nonlinear stability analysis involving all three modes, which is beyond of the scope of this paper.

For $x_c > 0$, Re_a becomes positive along curve O in figure 6. This means that the flow ascending near the axis is unstable with respect to the periodic disturbances when $\theta_c < 90°$. Since this flow is stable with respect to the non-oscillating disturbances, the oscillatory regimes can be stable in this case if the oscillatory bifurcation is supercritical (however, this again would require nonlinear analysis).

Since calculations show that the disturbance velocity rapidly decays from the surface to the axis at a fixed r, these neutral modes are localized near the $x = x_c$ surface. Therefore, a tentative physical interpretation of the oscillatory regimes is that the ascending-near-axis flow generates (steady) near-surface waves. The inset in the upper part of figure 6 shows a streamline the secondary $\ln r$-periodic flow.

The three-dimensional centre manifold occurs also on curve F_2 in figure 6.

4.4.3. *Triple neutral point*

As x_c increases along the right-hand branch of O in figure 6, $|\alpha_i|$ decreases and becomes zero at point T positioned exactly on curve F_2. The periodic neutral curve terminates at T, and there are three merged eigenvalues $\alpha = 0$: one exists owing to the fold F_2, and the other two result from the complex conjugate pair $\pm \mathrm{i}\alpha_i$ of the oscillatory branch O. Figure 10 shows the spectrum metamorphoses in the vicinity of the triple point T as x_c varies. Figure 10(*a*) corresponds to $x_c < x_{cT}$, where $x_{cT} = -0.193$ *is the* x_c value at T. There are one real (F_2) and two imaginary (O_1 and O_2) neutral points corresponding to the intersection of the dashed and solid curves with line $\alpha_r - 0$ in figure 10(*a*). Figure 10(*b*) corresponds to $x_c = x_{cT}$, where points O_2 and F_2 merge and where point O_2 itself is associated with two eigenvalues $\alpha = \pm \mathrm{i}\alpha_i$ which merge and become zero in figure 10(*b*). The solid line has an inflection point and the horizontal slope at $\alpha_r = 0$. For $x_c > x_{cT}$, the dashed curve separates into two disconnected branches (figure 10*c*). Each of the separated branches terminates at the local maximum and minimum of the solid curve. Point O_1 in figure 10(*c*) corresponds to the left-hand branch of curve O for $x_c > x_{cT}$ in figure 6.

Another striking feature is the existence of a continuum spectral component at $x_c = 0$.

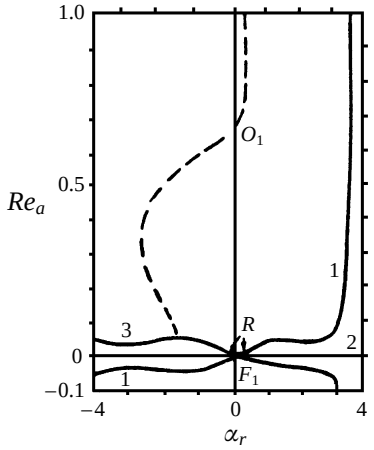

FIGURE 11. A spectrum transformation near the point $x_c = J_1 = 0$ in figure 6. ——, Real α at $x_c = -0.01$ (curve 1), 0 (curve 2), and 0.01 (curve 3).

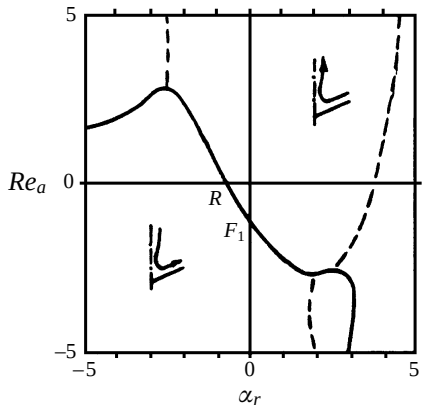

FIGURE 12. The dependence of ——, real α and – – –, α_r of complex α on the axial velocity at $x_c = 0.4$. The instability at fold F_1 is due to inner disturbances as path RF_1 shows.

4.4.4. *Continuous spectrum*

It can be seen in figure 9 that the upper solid curve is positioned near line $Re_a = 0$. Our calculations show that as $x_c \to 0$, this solid curve merges with line $Re_a = 0$. For $x_c > 0$, the solid curve is positioned above line $Re_a = 0$ for α less than some negative value. Solid curves 1, 2, and 3 in figure 11 show the calculated results for real eigenvalues at $x_c = -0.01$, 0, and 0.01, respectively. It appears that any real α is an eigenvalue for the problem for the still fluid at $x_c = 0$. The reason for this continuous spectral component is twofold: the conservation law for the flow force and the symmetry for the still fluid at $x_c = 0$.

4.4.5. *The instability for* $x_c > 0$

The periodic instability disappears as x_c exceeds 0.02. The eigenvalue spectrum becomes comparatively simple, as figure 12 shows for $x_c = 0.4$. Again, the solid curve represents real α and the dashed curves show α_r for complex-conjugate eigenvalues. The solid curve intersects line $\alpha_r = 0$ at F_1 which corresponds to fold (curve F_1 in figure 6). For $Re_a < 0$, the flow diverges near the cone surface (see the inset in the lower part

of figure 12). When one moves along the solid curve from R to F_1 in figure 12, the flow becomes unstable when the curve passes through line $\alpha_r = 0$. To clarify the nature of the growing disturbances, consider the fluid at rest, i.e. $Re_a = 0$. For the sake of the physical reasoning, we suppose that the fluid at rest is stable. The eigenvalue corresponding to the smallest $|\alpha_r|$ is real with $\alpha < 0$ (see point R in figure 12), which means that this disturbance originates near the cone apex and decays as r increases. As Re_a decreases, this spectral branch intersects line $\alpha_r = 0$, which means that the disturbance originating near the apex increases with r. Therefore, the diverging flow is unstable with respect to inner disturbances (coming from the near-apex region). This instability leads to flow separation from the surface and to transition from the flow pattern shown in the lower part of figure 12 to the flow pattern shown in the upper part.

Thus, the hysteretic transitions for $x_c < 0$ are due to the outer disturbances, whereas jump flow separation from the surface $x = x_c > 0$ occurs due to the inner disturbances. The oscillatory instability is due to the global disturbances.

Stability features crucially depend on boundary conditions at the surface, $x = x_c$, and on the choice of which flow characteristics serve as control parameters. If Re (instead of J_1) is a control parameter, then there are no folds and the solution is unique as figure 5 shows – in which case, however, another intriguing instability emerges related to swirl generation.

5. The instability nature of swirl bifurcation

5.1. *Possible mechanisms for appearance of swirl*

The generation of swirl due to symmetry breaking in primarily swirl-free flows is at first sight enigmatic. Without swirl forcing, the conservation of angular momentum excludes such an event. Nevertheless, there are experimental observations of swirl development without any obvious forcing when Reynolds number Re (characterizing the primary swirl-free flow) exceeds some threshold value Re_{cr} (Bojarevics *et al.* 1989; Fernandez de la Mora *et al.* 1991). These observations stimulated our theoretical studies of conical solutions of NSEs. While Shtern & Barrero (1995*a*) addressed conical flows only, here we study steady (§5) and unsteady (§7) disturbances of these flows.

Note that swirl cannot appear without a torque to counter the frictional resistance of walls in these experiments. The two crucial questions are (*a*) where is this source of the angular momentum, and (*b*) why does it influence the flow significantly only for $Re > Re_{cr}$? Although the conical model is a strong idealization of the practical flows, the following stability studies help to answer questions (*a*) and (*b*). To recognize where the swirl source is located and to understand why this source is 'locked' for $Re < Re_{cr}$ and 'unlocked' for $Re > Re_{cr}$, one must study the instability with respect to swirl disturbances. Shtern & Barrero (1995*b*) reported some preliminary stability results concerning electrosprays and Shtern (1995) treated a closely related problem on magnetic field pumping. Below, the stability of both one- and two-phase flows, driven either by surface stresses or by body forces, is studied in detail.

5.2. *General features of swirl disturbances*

It is possible to study axisymmetric swirl disturbances separately from meridional disturbances if the basic flow is swirl-free. At $m = 0$ and $\Gamma_b \equiv 0$, equation (6*c*) decouples and appears thus:

$$(1-x^2)\,\Gamma_d'' = [\alpha u_b + \alpha - \alpha^2]\,\Gamma_d - y_b\,\Gamma_d'. \tag{33}$$

The boundary condition on the axis is $\Gamma_d(1) = 0$ (see (7*b*)). According to §2.4, the condition at $x = x_c$ is either the no-slip, $\Gamma_d = 0$ (8*b*), or the zero shear stress, $(1-x^2)\Gamma'_d + 2x\Gamma_d = 0$ (10*b*). However, we will now show that there is no swirl bifurcation for the no-slip condition. Note that bifurcation of swirl occurs at $\alpha = 0$. In this neutral case, integration of (33) yields

$$\Gamma'_d = \Gamma'_d(x_0) \exp - y_b(1-x^2)^{-1}\,\mathrm{d}x\ , \tag{34}$$

where the integration runs from x_0 to x, x_0 being any value in the interval, $(x_c, 1)$. If $\Gamma_d(1) = \Gamma_d(x_c) = 0$, then Γ_d has its extremum inside $(x_c, 1)$ – at x_e where $\Gamma'_d = 0$. Choosing $x_0 = x_e$ in (34) yields $\Gamma'_d \equiv 0$ and, therefore, $\Gamma_d \equiv 0$. Thus, no non-trivial solution exists at $\alpha = 0$. Therefore, we only consider the stability study here under the stress-free condition for swirl disturbances.

To reveal other restrictions, it is useful to introduce a new function T, such that

$$\psi = -2(1-x^2)\,T'/T. \tag{35}$$

Then (4*a*) yields the equation for T,

$$T'' + \tfrac{1}{2}(1-x^2)^{-2} F T = 0, \quad \text{with conditions} \quad T'(x_c) = 0, \quad T(x_c) = 1. \tag{36}$$

The first condition follows from (10*a*) and (35); the second is a normalization. Substituting (35) into (34) (recall that $y_b = -\psi$) gives $\Gamma'_d = \Gamma'_d(x_0)/T^2$. Then, applying $x_0 = x_c$ and normalization $\Gamma_d(x_c) = 1$, using (10*b*), and integrating from $x = x_c$ to $x = 1$, we get

$$S(Re) \equiv \Gamma_d(1) = 1 - 2x_c(1-x_c^2)^{-1} \int T^{-2}\,\mathrm{d}x. \tag{37}$$

For $x_c \leqslant 0$, (37) shows that $\Gamma_d(1) \geqslant 1$; i.e. the condition $\Gamma_d(1) = 0$ cannot be satisfied. Thus, no swirl bifurcation occurs for $\theta_c \geqslant 90°$. Note that the free surface, in contrast, is apparently flat in the experiment by Bojarevics *et al.* (1989) where the swirl accumulation is observed. While this may indeed be a limitation of the model, the surface in the experiment may not be exactly flat, e.g. owing to the Zeleny–Taylor effect; the occurrence of bifurcation at high but finite Re_{cr} may be due to θ_c being slightly less than 90°.

For $F \leqslant 0$, (36) yields $T \geqslant 1$, and (37) yields $\Gamma_d(1) \geqslant (1-x_c)/(1+x_c) > 0$. Therefore, again $\Gamma_d(1) = 0$ cannot be satisfied. On the other hand, (36) with $F \leqslant 0$ yields $T' \geqslant 0$; then (35) shows $\psi \leqslant 0$. A basic flow with $\psi \leqslant 0$ moves to the cone apex along the axis and goes to infinity along the surface, and our analysis shows that swirl bifurcation cannot occur in a flow diverging near the surface. This agrees with the observations by Bojarevisc *et al.* (1989), that swirl appears in the converging-near-surface flow (see figure 2 and §1.2) as the electric current J_t exceeds 15 A, but does not appear in the diverging flow even at $J_t = 1500$ A.

There exists an eigenvalue, $\alpha = -1$, which, used to integrate (33), yields

$$(1-x^2)\,\Gamma'_d + (2x + y_b)\,\Gamma_d = 0. \tag{38}$$

The integration constant is zero owing to $\Gamma_d(1) = 0$. Since $y_b(x_c) = 0$, the stress-free condition (10*b*) is also satisfied. Integration of (38) from $x = x_c$ with the normalization, $\Gamma_d(x_c) = 1$ gives the eigenfunction. Thus, the eigenvalue $\alpha = -1$ is independent of the basic flow and the cone angle.

The physical reason for this independence is the conservation of angular momentum (see §3.2.1 for the $\alpha = -1$ universality for swirl disturbances of the still fluid). Consider

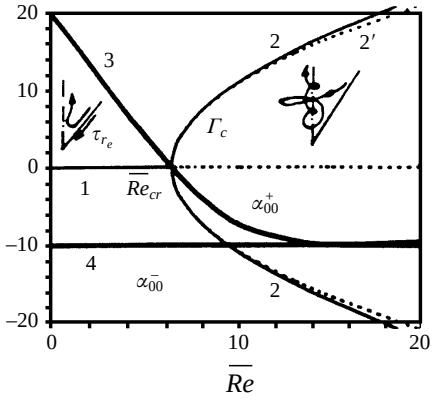

FIGURE 13. The pitchfork bifurcation of swirl (curves 1 and 2) at $\overline{Re}_{cr} = 6.3$ and the leading eigenvalues (curves 3 and 4 show $10 \times \alpha$) versus the Reynolds number $\overline{Re}$ for the flow inside the $\theta_c = 45°$ cone, driven by the radial surface stress $\tau_{r\theta}$. The insets show schematics of the primary (left) and secondary (right) flows. Curve 2′ shows the circulation Γ_c in a weakly nonlinear approximation (§7.2.4).

a control surface consisting of two conical and two spherical surfaces. Since there are no body forces generating swirl, the angular-momentum flux through the entire control surface is zero. The flux per unit area of a conical surface,

$$\Pi_{\theta\phi} = \rho v_\theta v_\phi - \rho\nu r^{-1} \sin\theta \, \partial/\partial\theta (v_\phi/\sin\theta) = \rho\nu^2 (r\sin\theta)^{-2} [(1-x^2)\,\Gamma_d' + (2x+y_b)\,\Gamma_d],$$

is zero due to (38). Therefore, the flux through the spherical parts of the control surface is also zero. Since $\alpha = -1$ relates to the inner mode, the universality means that the flux, given on the inner boundary of the similarity region, is the same for any spherical surface, $r = \text{const}$. Numerical calculations show that other inner disturbances decay even faster than the above mode as r increases.

Thus, we find that in general no swirl bifurcation occurs (i) for the no-slip, (ii) for $\theta_c \geqslant 90°$, and (iii) for flows diverging near the surface. Taking these general features into account, we restrict the following stability analysis to flows converging near the conical surface with $\theta_c < 90°$. The inner disturbances of swirl decay as r increases and the smallest decay rate corresponds to $\alpha = -1$ (a universal eigenvalue). In contrast, we show below that certain outer disturbances grow as r decreases: those in flows converging near the free surface with $\theta_c < 90°$.

5.3. *Instability of flows driven by surface stresses*

5.3.1. *One-phase flow*

To calculate the eigenvalue spectrum for swirl disturbances, we integrate (33) from $x = x_c$ to $x = x_f = 0.9999$. The initial conditions are $\Gamma_d(x_c) = 1$ (normalization) and $\Gamma_d'(x_c) = -2x_c/(1-x_c^2)$ to satisfy the stress-free condition (10). Then we adjust α to satisfy $\Gamma_d(1) = \Gamma_d(x_f) + (1-x_f)\,\Gamma_d'(x_f) = 0$.

Figure 13 shows the numerical results for a flow inside a cone of $\theta_c = 45°$. The inset on the left-hand side of figure 13 is a schematic of the primary flow driven by shear stress $\tau_{r\theta}$ applied on the surface. Line 1 represents the primary flow, which is swirl-free. The thick curves show swirl-disturbance eigenvalues, α_{00}^{+} (curve 3) and α_{00}^{-} (curve 4), corresponding to minimum $|\alpha|$ (enlarged 10 times in figure 13). At $Re = 0$, they coincide with those for the still fluid (see (18) for $n = 0$) and are universal with respect to θ_c (see §3.3.1 and figure 3).

The eigenvalue $\alpha_{00}^{-} = -1$ is universal with respect to Re as well, but as $|Re|$ increases,

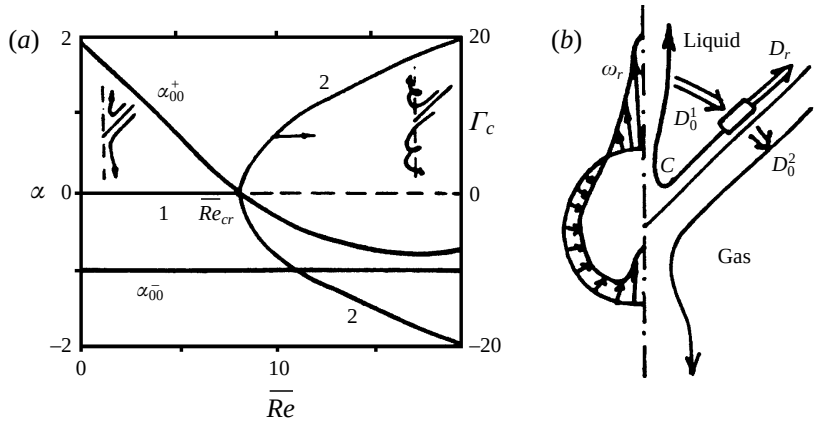

FIGURE 14. (*a*) As in figure 13 but with the liquid flow inside and the gas flow outside the cone. $\overline{Re}_{cr} = 7.79$. (*b*) Schematic of the angular momentum fluxes (right-hand side) and of the radial vorticity distribution (left-hand side).

α_{00}^{+} decreases and changes its sign at $Re = Re_{cr} = -6.3$. The value of Re is negative because the flow converges to the origin, i.e. the radial velocity is negative on the surface. It is convenient to introduce $\overline{Re} = -Re$. As $\overline{Re}$ increases, α_{00}^{+} approaches α_{00}^{-} (but remains larger), reaches its minimum, and then increases. The supercritical pitchfork bifurcation of the secondary swirling flows occurs at $\overline{Re} = \overline{Re}_{cr}$. Solid curve 2 shows circulation at surface Γ_c as a function of $\overline{Re}$ for the secondary flows. The inset on the right-hand side of figure 13 is a schematic of this self-swirling flow (see Shtern & Barrero (1995*a*) for a more detailed description of the secondary flow).

Thus, the appearance here of swirl relates to outer disturbances decaying for $\overline{Re} < \overline{Re}_{cr}$ and growing for $\overline{Re} > \overline{Re}_{cr}$ as r decreases. The maximum principle imposes itself strongly in this situation: circulation must have its maximum value at the boundary of the flow region for incompressible fluid with uniform physical properties. Although circulation of the growing disturbance increases as r decreases, its maximum is located on the boundary. In contrast, if the fluid properties are not uniform, then circulation can reach its maximum inside a flow region as we show below.

5.3.2. *Two-phase flow*

Here we consider a similar primary motion driven by stress $\tau_{t\theta}$ as in the above section, but now there is also a gas flow outside the liquid cone of $\theta_c = 45°$ (for basic flows, see Shtern & Barrero 1995*a*). For swirl disturbances, (33) is applied in both the media. The swirl velocity and shear stress must be continuous across the interface, $\theta = \theta_c$, that yield the conditions,

$$\left.\begin{aligned} (1-x_c^2)\,\Gamma_g'(x_c) + 2x_c\,\Gamma_g(x_c) &= r_{\mu\nu}[(1-x_c^2)\,\Gamma_l'(x_c) + 2x_c\,\Gamma_l'(x_c)], \\ \Gamma_g(x_c) &= r_\nu\,\Gamma_l(x_c), \quad r_\nu = \nu_l/\nu_g, \quad r_{\mu\nu} = \rho_l\,\nu_l^2/\rho_g\,\nu_g^2. \end{aligned}\right\} \tag{39}$$

The subscripts g and l refer, respectively, to the gas and liquid phases. Dimensional characteristics can be found with the help of (2) using the gas and liquid densities and viscosities in the corresponding flow regions. Conditions (39) are valid both for disturbances and for the secondary established regime.

Describing the numerical procedure for the stability study, equation (33) is integrated from $x = x_c$ in both directions, using $\Gamma_l(x_c) = 1$, a tentative value of $\Gamma_g'(x_c)$, and (39) to find $\Gamma_l'(x_c)$ and $\Gamma_g(x_c)$. Then we adjust $\Gamma_g'(x_c)$ to satisfy $\Gamma_g(-1) = 0$, and seek a value of α which satisfies $\Gamma_l(1) = 0$. In our calculations, the liquid is heptane

($\nu_l = 0.611 \times 10^{-6}$ m^2 s^{-1}, $\rho_l = 684$ kg m^{-3}) and the gas is air ($\nu_g = 14.8 \times 10^{-6}$ m^2 s^{-1}, $\rho_g = 1.21$ kg m^{-3}) at the reference temperature 20 °C, which yields $r_\nu = 0.0413$, $r_{\mu\nu} = 0.964$. One reason for such a choice is the common application of electrospray to fuel atomization.

Figure 14(*a*) shows the calculation results where values of $\overline{Re}$ and Γ_c are based on the liquid viscosity. The results are similar to those in figure 13, the difference being that $\overline{Re}_{cr} = 7.79$ is larger, and the growth rate, $|\alpha_{00}^+|$ for $\overline{Re} > \overline{Re}_{cr}$, is smaller, than those for the one-phase case. Moreover, the established circulation of the secondary regime is smaller in the two-phase flow. The physical reason of these (rather weak) effects of the gas flow is that the gas consumes part of the angular momentum and thus weakens both the swirl instability and the swirl of the secondary liquid flow.

Figure 14(*b*) illustrates the instability mechanism. There are the angular momentum fluxes for a small near-interface volume of the liquid denoted by the rectangle. The symbol C marks the convection of the angular momentum along a streamline, where circulation would be constant in an inviscid flow. Since the streamline approaches the axis, a drastic increase occurs in the swirl velocity and, especially, in the radial vorticity. A typical dependence of the radial vorticity on the polar angle θ at a fixed r appears on the left-hand side of figure 14(*b*). A sharp peak of vorticity near the axis induces viscous diffusion and hence the angular momentum transfer across streamlines from the axis to the interface (D_θ^l in figure 14*b*). This transfer increases circulation of the liquid element. The diffusion in the radial direction, D_r, and from the liquid to the gas, D_θ^g, remain to be considered. The latter fluxes decrease circulation of the liquid element. According to our results, the losses, $D_r + D_\theta^g$, dominate the gain, D_θ^l (as to be expected at low Re), and Γ_c decreases monotonically as r decreases for $\overline{Re} < \overline{Re}_{cr}$. However, for $\overline{Re} > \overline{Re}_{cr}$, D_θ^l dominates $D_r + D_\theta^g$ such that Γ_c increases as r decreases, until a nonlinear saturation occurs.

The saturation occurs because the centrifugal action of a strong swirl slows the meridional motion near the axis (moreover, the axial velocity can reverse; see Shtern & Barrero 1995*a*). This action moves the streamline away from the axis, whereupon the vorticity decreases. As a result, D_θ^l decreases; it reaches a balance with $D_r + D_\theta^g$; this balance corresponds to the secondary similarity regime. Finally, for the viscous vicinity of the origin, the similarity motion becomes a stagnation flow, and Γ_c falls to zero at $r = 0$.

The maximal value of circulation occurs inside the flow region for $\overline{Re} > \overline{Re}_{cr}$, which is not too striking since the maximum principle is not valid for a non-uniform medium. As r_ν and $r_{\mu\nu}$ go to zero, the two-phase problem is reduced to that of a single-phase (liquid).

The very moderate difference in the results between the two- and one-phase cases (compare figures 13 and 14*a*) arises from the relatively small role of the gas flow, the gas density being much smaller than the liquid density. Therefore, we consider further only one-phase flows.

5.4. *Instability of flows driven by body forces*

One motivation for the study in this section is the experiment by Bojarevics *et al.* (1989) mentioned in §§1.1 (figure 2), 1.2 and 5.1. To explore these self-swirling phenomena, Shtern & Barrero (1995*a*) have considered the following idealized problem. The infinite cone, $\theta \leqslant \theta_c$, of a conducting liquid has the stress-free surface, $\theta = \theta_c$. An electric current is issued radially from the cone tip with density, $j_r = J_t/[2\pi r^2(1-x_c)]$. According to the equation, $\boldsymbol{\nabla} \times \boldsymbol{B} = 4\pi \boldsymbol{j}$, the current induces the magnetic field, $B_\phi = 2J_t[r(1-x_c)]^{-1}[(1-x)/(1+x)]^{1/2}$. The electromagnetic force, $\boldsymbol{F} = \boldsymbol{j} \times \boldsymbol{B}$, acts along the

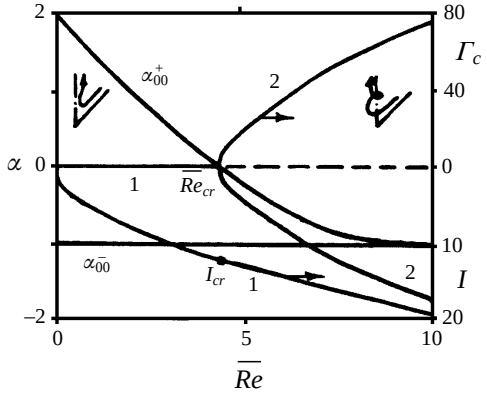

FIGURE 15. As figure 13, but for the flow driven by the electromagnetic body force. $\overline{Re}_{cr} = 4.24$. Curve I shows the relation between the total electric current and the radial velocity at the surface; $I_{cr} = 12.7$.

meridians. For convenience, we introduce the dimensionless total current $I = J_t(\frac{1}{2}\pi\rho\nu^2)^{-1/2}$. It then follows that the dimensionless force is

$$f_\theta = -\tfrac{1}{2}I^2(1-x_c)^{-2}[(1-x)/(1+x)]^{1/2}. \tag{40}$$

This force, instead of contributing to equations for disturbances, drives the basic flow. It appears that $f_b = f_\theta$ in (4*b*). Considering a swirl-free basic flow, i.e. $\Gamma \equiv 0$, substituting (40), and integrating (4*b*) under conditions (7*a*) and $F'(x_c) = 0$, we get

$$F = \tfrac{1}{2}I^2(1-x_c)^{-2}\{[(1+x)^2+(1-x)^2(1+x_c)/(1-x_c)]\ln[(1+x)/2]+2-2x-\tfrac{1}{2}(1-x)^2\}. \tag{41}$$

Applying (41) in (4*a*) and integrating from $x = x_c$ with $\psi(x_c) = 0$, we find the basic solution.

Here we study the instability of this basic solution to steady swirl disturbances. Substituting the basic solution in (33), and solving (33) under the same conditions and in the same manner as in §5.3.1, we obtain the results shown in figure 15. The notations in figure 15 are the same as in figure 13. For ease of comparison, again $\overline{Re}$ is used as the abscissa in figure 15, and curve I shows the relation between the total electric current and the radial velocity at the surface.

Again, the instability and bifurcation of the secondary swirling regime occur owing to the outer disturbances, as curve α_{00}^{+} indicates in figure 15. The critical parameters are $\overline{Re}_{cr} = 4.24$, $I_{cr} = 12.7$. Note that $\overline{Re}_{cr}$ is smaller than that in the previous problems. One reason may be that the body forces induce the flow. Our calculations reveal that the instability and bifurcation occur even if one uses the no-slip condition, i.e. $Re = 0$, for the basic flow (but not for swirl disturbances). We do not show details of these calculations here since the no-slip condition for the meridional motion and the stress-free condition for the swirl seem physically artificial.

5.5. *Mechanism of swirl accumulation*

The outer disturbances are responsible for swirl bifurcation in all three of the above examples. What does it mean from the physical point of view? Our interpretation is that there is a remote source of the angular momentum. The source can be due to some asymmetric roughness or skewness of the capillary tube in electrosprays. In the electro-vortex flow of mercury, the source may be also due to some roughness of the wall or due to a stray (e.g. Earth's) magnetic field. This source, being very weak, does not

provide visible or measurable swirl when meridional motion is slow. However, for $\overline{Re} > \overline{Re}_{cr}$, a mechanism resembling a pump begins to work (see §5.3.2 and figure 14*b*).

The meridional diffusion D_θ plays the leading role in the accumulation mechanism as explained in §5.3.2. Note the difference between the equation for circulation and the advection–diffusion equation (which governs temperature and concentration fields). Temperature, like Γ, is conserved along streamlines and can be uniform in an inviscid conduction-free flow. However, diffusion effects are different for temperature and Γ. A small heat conductivity does not affect a uniform temperature field, while a small viscosity destroys a uniform Γ to eliminate the delta-function singularity of vorticity on the axis of symmetry, and, therefore, causes the transfer of Γ from the axis.

The total outcome of the angular momentum due to the radial diffusion is proportional to the cone angle, θ_c (figure 14*b*). In contrast, as θ_c increases, $\mathrm{d}\Gamma/\mathrm{d}\theta$ and, therefore, the meridional viscous transfer of swirl, decreases. This explains why there is no swirl bifurcation for $\theta_c > 90°$ in the single-phase flows. In the two-phase flow, the gas flow contributes a very small amount of the angular momentum due to a huge liquid/gas density ratio. For this reason, only the value of the angle enclosing liquid region is crucial for instability. However, if θ_c is very small, the convergence of streamline near the surface is weak, decreasing the accumulation effect. Moreover, for small θ_c, the gas flow consumes a larger share of the angular momentum than that for large θ_c. Therefore $\overline{Re}_{cr}$ reaches its minimum at an intermediate θ_c value (near 45°) in the two-phase flow.

Thus in all the problems studied, swirl bifurcation occurs owing to instability with respect to the outer disturbances. The circulatory meridional flow, converging near the surface, works as a pump taking the angular momentum from a weak remote source and accumulating swirl in the similarity region (§7.2).

6. Azimuthal instability

While studying the instabilities related to jump transitions and swirl appearance in §§4–5, we have treated the meridional and swirl disturbances separately since the corresponding equations are decoupled. Now we consider the case when these disturbances are coupled and lead to azimuthal symmetry breaking. In contrast to swirl bifurcation, which occurs in the converging-near-surface flows, the azimuthal symmetry breaking of 3D flow occurs in the diverging-near-surface flows. Although this instability was observed about 150 years ago (see §1.2), its theory has been developed only recently. First, supercritical bifurcation of the secondary steady ϕ-dependent solutions was found for a number of diverging flows (Shtern & Hussain 1993). Then a bifurcation cascade – decreasing flow scales in ϕ and θ – was revealed in the Marangoni convection (Shtern & Hussain 1994). This explains the observation by Pshenichnikiov & Yatsenko (1974) that the number of azimuthal vortices increases with *Re*. In the present paper, we study the origin of disturbances (responsible for the divergent instability), considering three problems with different boundary conditions and forcing. First we address the Squire–Wang flow.

6.1. *Squire–Wang flow*

Consider a viscous fluid flow in a half-space, $x > 0$, induced by the shear stress, $\tau_{r\theta} \sim 1/r^2$, acting on the surface. Solution (30) is valid for this problem with the relation, $Re_\tau = 2Re$, where $Re_\tau = r^2\tau_{r\theta}/\rho\nu^2$. Wang (1991) has interpreted such a flow (for $Re > 0$) as a model of oceanic motion induced by oil spreading after a tanker spillage. The symmetry breaking of this flow, i.e. bifurcation of the steady secondary flows with azimuthal cells was found by Shtern & Hussain (1993). There is an infinite set of critical

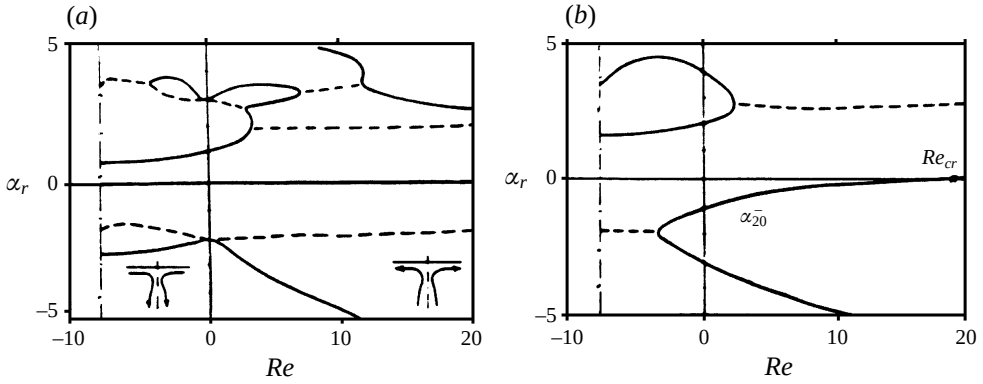

FIGURE 16. An eigenvalue spectrum for azimuthal disturbances in the Squire–Wang flow. Azimuthal wavenumber (*a*) $m = 1$, and (*b*) $m = 2$. The intersection of curve α_{20}^- with line $\alpha_r = 0$ at $Re = Re_{cr}$ indicates instability (see curve α_{20}^- also in figure 17). The insets show flow patterns for $Re < 0$ and $Re > 0$. ——, real α; – – –, complex α.

Reynolds numbers Re_{cr}; the minimum ($Re_{cr} = 18.9$) corresponds to azimuthal wavenumber $m = 2$. However, the origin of disturbances responsible for this bifurcation has been unclear so far; here we address this question.

To find eigenvalues α, we integrate (6) under conditions (8*b*) and (10*b*). Figure 16 shows the numerical results for the azimuthal wavenumber (*a*) $m = 1$ and (*b*) $m = 2$. Since we seek an α_r which passes through zero as Re varies, only a few eigenvalues with $|\alpha_r|$ close to zero are presented. No intersection of curves $\alpha_r(Re)$ with the line, $\alpha_r = 0$, occurs for $Re < 0$; therefore, there is no azimuthal instability in the converging flow.

Figure 16(*a*) shows how the degeneracy of the spectrum at $Re = 0$ disappears for $Re \neq 0$. There are three merged eigenvalues, $\alpha = 3$ and $\alpha = -2$, at $Re = 0$. For $Re \neq 0$, they split into one real and two complex-conjugate eigenvalues. The dashed curves show the real parts of complex α in figure 16. One can see a number of transformations of real eigenvalues into complex ones and vice versa. (To calculate merging and reconnection of eigenvalues, we use the Newton procedure modified for the case of multiple roots.) Unlike the situation in the problem studied in §4.4, the reconnections do not relate to the instability here.

The eigenvalue, $\alpha = \alpha_{10}^- = 0$, exists for any Re (figure 16*a*). At $Re = 0$, α_{10}^- corresponds to a source of the momentum at the origin (see §3.2.2). Since such a source is absent in the problem considered, no bifurcation occurs at $\alpha_{10}^- = 0$. No spectral curve intersects the line, $\alpha_r = 0$, in figure 16(*a*), and, therefore, there is no azimuthal instability at $m = 1$.

In contrast, figure 16(*b*) shows that branch α_{20}^-, which starts from $\alpha = -1$ at $Re = 0$, crosses the line, $\alpha_r = 0$, at $Re = Re_{cr} = 18.9$ (see also curve α_{20}^- in figure 17). This agrees with the result on bifurcation at $Re = 18.9$ in Shtern & Hussain (1993). The agreement of the instability and bifurcation results, and coincidence of the numerical results with the analytical solutions at $Re = 0$ serves to check our calculations.

Figure 17 shows only the spectral branches relevant for the instability. The scale of the ordinate in figure 17 serves to 'blow up' regions near the intersection of the curves with the line, $\alpha_r = 0$ (compare figures 16*b* and 17). Besides α_{20}^-, branches α_{30}^- and α_{40}^- also appear in figure 17. All these branches cross the line $\alpha_r = 0$ also at the Re where bifurcations of the secondary non-axisymmetric regimes occur (Shtern & Hussain 1993). The new result, here is that azimuthal symmetry breaking is due to inner disturbances.

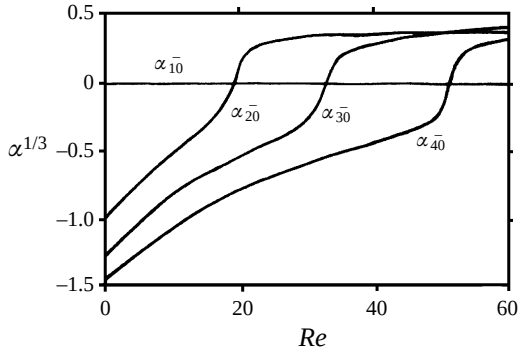

FIGURE 17. The eigenvalues α^{-}_{m0} ($m = 1$, 2, 3, and 4) *vs.* the Reynolds number for the Squire–Wang flow.

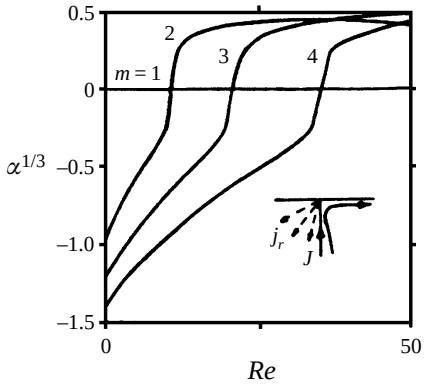

FIGURE 18. As in figure 17 but for the electro-vortex flow. The inset shows a typical streamline (right-hand side) and electric current distribution (left-hand side).

The interpretation of the basic flow of this section can differ from Wang's. Squire's solution describes well the Marangoni convection in the half-space induced by a point source of heat on the surface (Shtern & Hussain 1993). The above stability study addresses the particular case of the Marangoni convection where the Pradtl number is zero. Both Marangoni and Wang's flows are driven by surface shear stresses. To encompass a wider variety of flows and to show that the crucial reason for the azimuthal instability is flow divergence (but not a specific character of driving forces), we now consider two problems where body forces drive a flow.

6.2. *Diverging electro-vortex flow*

The basic flow is similar to that studied in §5.4, differing only by the arrangement of the electric current. The current is supplied here not by the outer electrode but by a wire positioned on the symmetry axis inside the flow region. The wire is electrically isolated everywhere except at its tip which touches the stress-free surface, $x = 0$. The current radially spreads downward from the tip to infinity. The left-hand part of the inset in figure 18 shows the current distribution and the right-hand part shows a typical streamline. We refer the reader to Bojarevics *et al.* (1989) for more details concerning the basic flow and show only the distribution,

$$f_\theta = \tfrac{1}{2} I^2 x (1 - x^2)^{-1/2}, \tag{42}$$

of the Lorentz force driving the flow. Using (42) in (4*b*) with (7*a*) and $F'(0) = 0$ yields

$$F = \tfrac{1}{4}I^2[(1+x)^2\ln(1+x)+(1-x)^2\ln(1-x)-(2\ln 2+1)\,x^2-(2\ln 2-1)]. \qquad (43)$$

Applying (43) in (4*a*) and integrating from $x = 0$ with $\psi(0) = 0$, we find the primary solution.

The numerical procedure for the instability study is similar to that in §6.1. The main plot of figure 18 shows eigenvalues α for the disturbances causing the instability. The numbers near the curves are the values of m. The Reynolds number Re is the dimensionless surface velocity which is proportional to the electric current squared: $Re = I^2(2\ln 2-1)/4$.

The numerical results coincide with the analytical solutions (21) corresponding to $\alpha^-_{m0} = 1-m$ at $Re = 0$. Eigenvalue $\alpha^-_{10} = 0$ at $m = 1$ is universal with respect to Re, but no bifurcation relates to this 'neutral' mode In contrast, the instability and bifurcation occur as curves 2, 3, 4 (and so on) intersect the line, $\alpha = 0$, at $Re = Re_{cr} = 10.9$, 21.2, and 35.4, respectively. The stress-free condition at the surface is crucial for this instability.

The following numerical experiment has been performed by way of verification. Introduce a parameter, say *par*, which governs the boundary condition. The stress-free condition occurs at $par = 0$ and the no-slip at $par = 1$. First, we calculate Re_{cr} at $par = 0$, and then gradually increase *par*. It appears that as *par* approaches 1, Re_{cr} goes to infinity. Thus, the no-slip condition suppresses the divergent instability if the flow diverges near the rigid boundary. However, if a flow diverges along a surface remote from a rigid boundary, the azimuthal instability does occur as the following example shows.

6.3. *Thermal convection*

The buoyancy force drives the basic flow in this section. The flow above a rigid cone, $x = x_c$, is induced by the temperature field corresponding to a quadruplet source of heat at the cone tip. The azimuthal symmetry breaking in the basic flow was found in Shtern & Hussain (1993). Here, we study the origin of disturbances causing the divergent instability. To avoid the coupling with the thermal problem and thus to simplify the following analysis, we restrict ourselves to the case of zero Pradtl number. Then the temperature distribution,

$$T = T_\infty + \gamma\vartheta(x)/r^3, \quad \vartheta = 3x^2-1,$$

is independent of the flow. Here T_∞ is an ambient temperature and γ is a characteristic of the thermal quadruplet intensity. The basic flow satisfies the no-slip condition at $x = x_c$, and it is governed by (4*a*) with

$$F = \tfrac{1}{4}Gr(1-x)^2[x(1+x)^2-x_c(1+x_c)^2],$$

where $Gr = \beta\gamma g/\nu^2$ is the Grashof number, β is the heat expansion coefficient and g is the acceleration due to gravity.

The inset in figure 19 shows a flow pattern (right-hand side) and a temperature distribution (left-hand side). The azimuthal instability occurs for negative Gr. This means that cooling occurs near the axis of symmetry and heating near the equatorial plane. For such a temperature distribution and rather sharp cones of $x_c < -\frac{1}{3}$, the motion is two-cellular with an annular conical jet flowing out between the cells.

The main plot of figure 19 shows neutral curves for disturbances with $m = 2$, 3 and 4. Which disturbance is the most dangerous, i.e. corresponds to the smallest $|Gr_{cr}|$, depends on x_c. It can be seen from figure 19 that $|Gr_{cr}|$ and m_{cr} increase with x_c. Since the annular jet attaches to the cone surface and the no-slip condition suppresses the

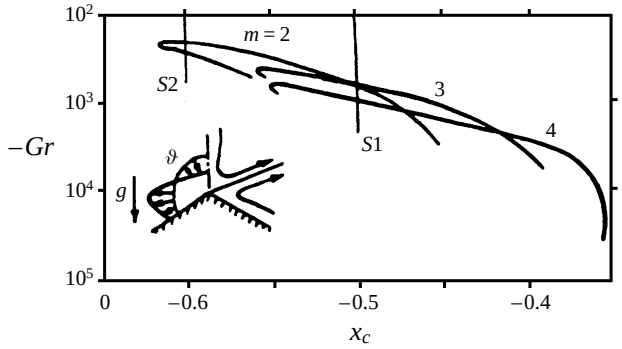

FIGURE 19. The neutral curves for azimuthal disturbances of $m = 2$, 3, and 4 in the thermal convection flow. The inset shows typical streamlines (right-hand side) and temperature distribution (left-hand side).

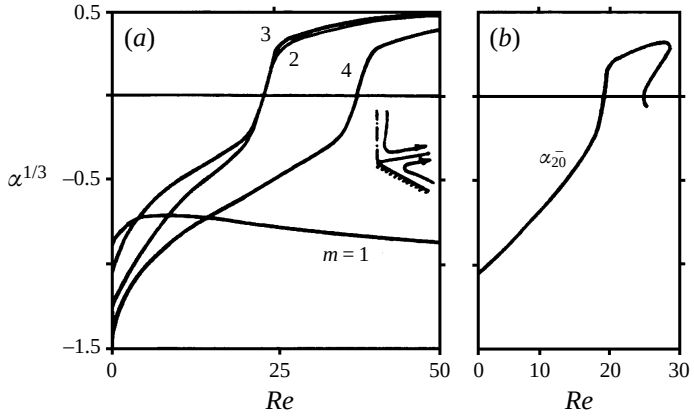

FIGURE 20. (*a*) The eigenvalues α_{m0}^- ($m = 1$, 2, 3, and 4) *vs.* *Re* based on the maximal radial velocity of the outflow at $\theta_c = 120°$ (section *S*1 in figure 19). (*b*) α_{20}^- *vs.* *Re* for section *S*2 in figure 19.

instability, both $|Gr_{cr}|$ and m_{cr} go to infinity as x_c approaches $-\frac{1}{3}$. The instability fails to occur also for x_c close to -1, because the annular jet approaches the symmetry axis and divergence of stream surfaces becomes too weak.

Figure 20 shows eigenvalues $\alpha(Re)$ at the cone angles: (*a*) $x_c = -0.5$ (see section *S*1 in figure 19) and (*b*) $x_c = -0.6$ (see section *S*2 in figure 19). The first value is chosen because curves 2 and 3 in figure 19 intersect at $x_c = -0.5$. The Reynolds number $Re = rv_{rs}/\nu$ at the abscissa of figure 20 is the dimensionless radial velocity v_{rs} on the conical surface, $x = x_s$, separating the flow cells; v_{rs} is close to the maximal radial velocity of the annular jet. The analytical relation, $x_s = -1-2x_c$, exists between the angles of the separation surface ($x = x_s$) and the boundary surface ($x = x_c$) for small $|Gr|$, while $x_s > -1-2x_c$ for large negative *Gr*.

At $Re = 0$, the eigenvalues coincide with those for the still fluid. Curve 1 in figure 20(*a*) does not cross the $\alpha = 0$ line. This means that no instability occurs with respect to the $m = 1$ disturbances. In contrast, curves 2–4 do intersect the $\alpha = 0$ line at *Re* values corresponding to the neutral curves in figure 19. The intersection of curves 2 and 3 in figures 19 and 20(*a*) means that the neutral manifold in the phase space is three-dimensional. The phase variables are amplitudes of azimuthal harmonics with $m = 2$ and 3, and their phase difference. In the three-dimensional case, a complex (chaotic) spatial flow pattern is possible for the secondary regime.

Section $S2$ in figure 19 is chosen because it intersects both the branches of the neutral curve for $m = 2$. Figure 20(b) shows the relation between α and Re for this case. The instability range exists between the intersection points of curve α_{20}^{-} with the $\alpha = 0$ line. Function $\alpha(Re)$ is not single-valued in figure 20(b) because Re is not a single-valued function of Gr at a fixed x_c.

Figure 20 shows that the divergent instability of the annular conical jet is caused by the inner disturbances. Since the jet is separated from the rigid cone, the no-slip condition at the cone boundary does not suppress this instability.

Although the three problems studied in §6 differ in their boundary conditions and type of forcing, the divergent instability relates to the inner disturbances in all of them. Therefore, it appears that the azimuthal symmetry breaking typically occurs owing to the disturbances originating from the inner boundary of the similarity region.

7. Temporal instability

7.1. *Small parameter technique*

7.1.1. *Equations for time-dependent disturbances*

To understand how the neutral steady modes found in §§4–6 relate to the temporal instability, consider time evolution in the vicinity of $Re = Re_{cr}$. Since the τ-derivative terms in (3) have the coefficient, $\exp(2\xi)$, time-dependent infinitesimal disturbances have no normal form with respect to ξ, making temporal analysis more difficult than that in §§4–6. To pursue the study, we exploit the fact that time evolution of growing modes is slow near $Re = Re_{cr}$ as these disturbances are steady at $Re = Re_{cr}$.

The disturbances allow the normal form with respect to τ and ϕ:

$$\left.\begin{aligned} u &= u_b(x) + u_d(x,\xi)\exp(\lambda\tau + \mathrm{i}m\phi) + \text{c.c.}, \quad y = y_b(x) + y_d(x,\xi)\exp(\lambda\tau + \mathrm{i}m\phi) + \text{c.c.}, \\ q &= q_b(x) + q_d(x,\xi)\exp(\lambda\tau + \mathrm{i}m\phi) + \text{c.c.}, \quad \Gamma = \Gamma_b(x) + \mathrm{i}\Gamma_d(x,\xi)\exp(\lambda\tau + \mathrm{i}m\phi) + \text{c.c.} \end{aligned}\right\} \tag{44}$$

Substituting (44) into (3) and neglecting nonlinear terms with respect to disturbances yields

$$u + u_\xi - m\Gamma/(1-x^2) - y_x = 0, \tag{45a}$$

$$\lambda u\exp(2\xi) - (1-x^2)u_{xx} + (2x - y_b)u_x - yu_{bx} - u_{\xi\xi} - u_\xi + u_b u_\xi - 2u_b u - 2q + q_\xi + (\mathrm{i}m\Gamma_b u - 2y_b y - 2\Gamma_b\Gamma + m^2 u)/(1-x^2) = 0, \tag{45b}$$

$$\lambda\Gamma\exp(2\xi) - (1-x^2)\Gamma_{xx} + u_b\Gamma_\xi - y_b\Gamma_x - \mathrm{i}\Gamma_{bx}y + \Gamma_\xi - \Gamma_{\xi\xi} - 2mu + mq + (\mathrm{i}m\Gamma_b\Gamma - 2mxy + m^2\Gamma)/(1-x^2) = 0, \tag{45c}$$

$$\lambda y\exp(2\xi) - (1-x^2)q_x + (1-x^2)(u_x - u_{x\xi}) + m\Gamma_{x\phi} + u_b y_\xi - y_b u_\xi - y_b u - u_b y + y_\xi - y_{\xi\xi} + [\mathrm{i}m\Gamma_b y + my_b\Gamma - 2x(y_b y + \mathrm{i}\Gamma_b\Gamma) + m^2 y]/(1-x^2), \tag{45d}$$

where subscript d is omitted. For neutral disturbances found in §§4–6, λ is zero at $Re = Re_{cr}$. Therefore, λ is close to zero in the vicinity of $Re = Re_{cr}$ and a small parameter expansion can be applied. The expansion allows transformation of (45) into a sequence of ODEs.

7.1.2. *Superposition of exponential functions*

Although (45) does not allow normal modes with respect to ξ, its solution can be represented as the sum of correlated exponential terms,

$$f(x,\xi) = \sum f_n(x,\alpha)\exp[(\alpha + 2n)\xi], \tag{46}$$

where $n = 0, 1, \ldots$, and f represents any function from u_d, y_d, q_d and Γ_d.

Introducing the vector, $\boldsymbol{U} = \{y, u, u_x, \Gamma, \Gamma_x, q\}$ and using (46), we reduce (45) to the compact form,

$$\boldsymbol{U}'_{dn+1}(x,\alpha) = L[\boldsymbol{U}_b(x)]\,\boldsymbol{U}_{dn+1}(x,\alpha) + \lambda P[\boldsymbol{U}_{dn}(x,\alpha)], \tag{47}$$

where the prime denotes differentiation with respect to x, L is a matrix whose coefficients depend on x (explicitly and through the basic flow denoted by $\boldsymbol{U}_b$), and P is an operator that transforms $\boldsymbol{U}$ into $\{0, 0, u, 0, \Gamma, y\}/(1-x^2)$. At $\lambda = 0$, (47) is identical to (6), but rewritten as a system of first-order differential equations.

The presence of $\boldsymbol{U}_{dn}(x,)$ in (47), coupling an infinite number of such systems, is a serious difficulty, but we are able to resolve it with the help fo the small parameter expansion near $Re = Re_{cr}$.

7.1.3. *Orthogonality condition*

Introduce the small parameter, $\varepsilon = Re - Re_{cr}$, and use the power expansion,

$$\lambda = \varepsilon\lambda_1 + \varepsilon^2\lambda_2 + \ldots, \quad \boldsymbol{U}_d = \boldsymbol{U}_{d0} + \varepsilon\boldsymbol{U}_{d1} + \ldots, \quad \boldsymbol{U}_b = \boldsymbol{U}_{b0} + \varepsilon\boldsymbol{U}_{b1} + \ldots, \tag{48}$$

Substituting (48) into (47) yields at the zeroth order $\boldsymbol{U}'_{d0} = L[\boldsymbol{U}_{b0}]\,\boldsymbol{U}_{d0}$ which coincides with (6). Its solution $\boldsymbol{U}_{d0}$ is a neutral mode. Term $\boldsymbol{U}_{b1}$ is the derivative of the basic solution with respect to Re and does not depend on disturbances. The first order yields

$$\boldsymbol{U}'_{d1} - L[\boldsymbol{U}_{b0}]\,\boldsymbol{U}_{d1} = L[\boldsymbol{U}_{b1}]\,\boldsymbol{U}_{d0} + \lambda_1 P[\boldsymbol{U}_{d0}]. \tag{49}$$

Note that the right-hand side (49) depends on $\boldsymbol{U}_{d0}$ and $\boldsymbol{U}_{b1}$ but not $\boldsymbol{U}_{d1}$. Therefore, $L[\boldsymbol{U}_{b1}]\,\boldsymbol{U}_{d0}$ and $P[\boldsymbol{U}_{d0}]$ are known at this stage, while λ_1 still must be found. Since the uniform problem, $\boldsymbol{U}'_{d1} - L[\boldsymbol{U}_{b0}]\,\boldsymbol{U}_{d1} = 0$, has a non-zero solution ($\boldsymbol{U}_{d1} = \boldsymbol{U}_{d0}$), the non-uniform equation (49) can be solved only if the orthogonality condition,

$$\{\boldsymbol{W}, L[\boldsymbol{U}_{b1}]\,\boldsymbol{U}_{d0} + \lambda_1 P[\boldsymbol{U}_{d0}]\} = 0, \tag{50}$$

is satisfied. Here $\{,\}$ denotes the scalar product,

$$\{\boldsymbol{W}, \boldsymbol{U}\} = \quad w_k\, u_k^c\, \mathrm{d}x,$$

(superscript c denotes complex conjugate, summation is required on $k = 1, \ldots, 6$, and integration runs from x_c to 1), and $\boldsymbol{W}$ is a non-zero solution of the adjoint problem,

$$\boldsymbol{W}' = L^a[\boldsymbol{U}_{b0}]\,\boldsymbol{W}. \tag{51}$$

[The matrix L^a is defined by relations $L^a_{ij} = -L^c_{ji}$.] Boundary conditions for $\boldsymbol{W}$ result from the requirement that $w_k\, u_k^c$ is zero at $x = x_c$ and $x = 1$ (see Appendix for detailed form of (51) and the boundary conditions for $\boldsymbol{W}$). For each neutral solution of (6), a non-trivial solution of (51) must exist to serve as a check of the calculations. The algorithm to find these solutions of (51) is similar to that for $\boldsymbol{U}_{d0}$. After finding $\boldsymbol{W}$, (50) yields

$$\lambda_1 = -\{\boldsymbol{W}, L[\boldsymbol{U}_{b1}]\,\boldsymbol{U}_{d0})\}/\{\boldsymbol{W}, P[\boldsymbol{U}_{d0}]\}. \tag{52}$$

If λ_1 is real, the temporal instability is monotonic, while complex λ_1 ($= \lambda_{1r} + \mathrm{i}\lambda_{1i}$) indicates oscillatory instability. For $\lambda_{1r} > 0$, instability occurs for $Re > Re_{cr}$. Thus, the calculation of λ_1 reveals (*a*) where the temporal instability occurs (for $Re > Re_{cr}$ or $Re < Re_{cr}$) and (*b*) the character (monotonic or oscillating) of time evolution for growing disturbances.

If the steady approach yields that only one neutral mode exists at $Re = Re_{cr}$, then the eigenvalue, $\lambda = 0$, is simple. Since the governing NSEs are real, complex λ can appear only by conjugate pairs, $\lambda = \lambda_r \pm \mathrm{i}\lambda_i$. Such a pair cannot develop for $Re \neq Re_{cr}$,

starting from a single eigenvalue, $\lambda = 0$ at $Re = Re_{cr}$. For this reason, the time evolution of the corresponding disturbances is monotonic.

However, if more than one steady neutral mode exists at $Re = Re_{cr}$, then eigenvalue $\lambda = 0$ is multiple and a complex conjugate pair of λ can appear for $Re \neq Re_{cr}$. Examples of multiple eigenvalues are cusp K and triple point T in figure 6, and the points where the neutral curves intersect in figure 19. In the vicinity of K, time-oscillating solutions are possible. Near the triple point and the intersection points, time dynamics can even be chaotic, as was experimentally observed near $Re = Re_{cr}$ by Pshenicnnikov & Yatsenko (1974) for the divergent instability in the Marangoni convection.

Now we consider the nonlinear spatiotemporal evolution of disturbances near swirl (§7.2) and fold (§7.3) bifurcation points. To this end we derive amplitude equations of the Landau–Ginzburg type applying orthogonality conditions which are similar to (50) but also involve nonlinear terms. While the linear technique described above is common, the amplitude equations are different for the fold and pitchfork (i.e. swirl) bifurcations.

7.2. *Evolution of swirl disturbances*

7.2.1. *Amplitude equation*

Here a weakly nonlinear approach is developed to study the spatiotemporal evolution and saturation of disturbances in the vicinity, $\overline{Re}\ (\equiv -Re) = \overline{Re}_{cr} + \varepsilon$. The swirl bifurcation is chosen as the first example since the technique is simpler in this case. In the leading order of magnitude with respect to ε, the growing disturbance is represented as the product, $A(\tau, \xi)\, \Gamma_0(x)$, where $\Gamma_0(x)$ is the eigenfunction corresponding to the neutral mode and amplitude A is governed by the nonlinear equation derived below. For axisymmetric flows, (3c) reduces to

$$(1-x^2)\,\Gamma_{xx} = u\Gamma_\xi - y\,\Gamma_x + \Gamma_\xi - \Gamma_{\xi\xi} - \Gamma_\tau \exp(2\xi). \tag{53}$$

We consider a solution of (59) for $\overline{Re} = \overline{Re}_{cr} + \varepsilon$ and use the expansion,

$$\Gamma = \epsilon^{1/2} A(\varepsilon\tau, f(\xi, \epsilon))\, \Gamma_0(x) + \varepsilon^{3/2} A_2(\varepsilon\tau, f(\xi, \epsilon))\, \Gamma_1(x) + \dots, \tag{54}$$

where A is of $O(1)$. The expansion (54) starts from the term of $O(\varepsilon^{1/2})$ because the saturated swirl is of $O(\varepsilon^{1/2})$, as curve 2 in figure 13 shows for the secondary flow. Since the neutral mode and the secondary flow are steady, A depends on 'slow' time $T = \varepsilon\tau$. The neutral solution is also ξ-independent, making A_ξ of $O(\varepsilon)$. However, A cannot depend only on the 'slow' variable, $\varepsilon\xi$, because (53) includes $\exp(2\xi)$. For this reason, $A_{\xi\xi}$ is of $O(\varepsilon)$, not of $O(\varepsilon^2)$.

For terms of $O(\varepsilon^{1/2})$, (53) and (54) yield the equation for the neutral mode Γ_0,

$$(1-x^2)\,\Gamma_0'' + y_{b0}\,\Gamma_0' = 0, \tag{55a}$$

which under the conditions,

$$\Gamma_0'(x_c) = -2x_c/(1-x_c^2)\,\Gamma_0(x_c), \quad \Gamma_0(1) = 0 \tag{55b}$$

has a non-trivial solution at $Re = Re_{cr}$ (§5.3.1); the solution is normalized here by $\Gamma_0(x_c) = 1$.

The meridional motion (involved in (53) through u and y) is a sum of the basic flow and disturbance,

$$y = y_b(x) + y_d(\varepsilon\tau, f(\xi, \epsilon), x),$$

(the expansions for u and q are similar to that for y). The dependence of the basic flow on Re is described by the expansion,

$$y_b = y_{b0}(x) + \varepsilon y_{b1}(x) + \dots,$$

with $u_b = y_b'$ following from (3d). Linear disturbances of the meridional motion of

$O(\varepsilon^{1/2})$ are decoupled from the swirl disturbances. These meridional disturbances have no growing modes at $Re = Re_{cr}$ and, hence, do not contribute to the amplitude equation. However, the meridional disturbances of $O(\varepsilon)$ owing to the nonlinear effect of the swirl do contribute; they are represented by

$$y_d = \varepsilon A_1^2 y_{d1}(x) + \dots,$$

where y_{d1} is the solution of the system,

$$y' = u, \tag{56a}$$

$$(1-x^2)\,u'' = (2x - y_{b0})\,u' - u'_{b0}\,y - 2u_{b0}\,u - 2q - (2y_{b0}\,y + \Gamma_0^2)/(1-x^2), \tag{56b}$$

$$(1-x^2)\,q' = (1-x^2)\,u' - y_{b0}\,u - y u_{b0} - x(2y_{b0}\,y + \Gamma_0^2)/(1-x^2), \tag{56c}$$

which follows from (3) for terms of $O(\varepsilon)$ (the subscript $d1$ is omitted). The boundary conditions are

$$y = 0, \quad u' = u_{b0}\,u + q \quad \text{at} \quad x = 1, \quad y = u = 0 \quad \text{at} \quad x = x_c. \tag{56d}$$

Since Γ_0 is known at this stage, (56) is a linear problem having a unique solution.

For terms of $O(\varepsilon^{3/2})$, (53) and (54) yield

$$A_2[(1-x^2)\,\Gamma_1'' + y_{b0}\,\Gamma_1'] = \varepsilon^{-1}[(1+u_{b0})\,A_\xi - A_{\xi\xi}]\,\Gamma_0 + A_T \exp(2\xi)]\,\Gamma_0 - (A y_{b1} + A^3 y_{d1})\,\Gamma_0'. \tag{57}$$

Although (57) involves ε, all terms have the same order of magnitude because A_ξ and $A_{\xi\xi}$ are of $O(\varepsilon)$. The uniform version of (57) (i.e. with the right-hand side being zero) coincides with (55*a*) and has the solution $\Gamma_1 = \Gamma_0$, under conditions (55*b*). For (57) to be solvable, its right-hand side must be orthogonal to the adjoint solution w. We derive the adjoint problem,

$$(1-x^2)\,w'' - (y_{b0} + 4x)\,w' - (u_{b0} + 2)\,w = 0, \quad w'(x_c) = 0,$$

$$4w' + (u_{b0} - 2)\,w = 0 \quad \text{at} \quad x = 1,$$

by multiplying (55*a*) by w, integrating by parts from $x = x_c$ to $x = 1$ and applying (55*b*). We start integration at $x = x_c$ with $w'(x_c) = 0$ using $w(x_c) = 1$ as normalization, and find $4w' + (u_{b0} - 2)\,w$ at $x = 1$ as a function of Re. Requiring that this function be zero at $Re = Re_{cr}$ serves as a check for the calculations.

Multiplying (57) by w and integrating from $x = x_c$ to $x = 1$ make the left-hand side zero, while the right-hand side becomes x-independent. The resulting equation for amplitude A is

$$A_T = \exp(-2\xi)\,[\gamma A - \delta A^3 + (A_{\xi\xi} - \beta A_\xi)/\varepsilon]. \tag{58}$$

where

$$\gamma = \int y_{b1}\,\Gamma_0'\,w\,\mathrm{d}x \Big/ \int \Gamma_0\,w\,\mathrm{d}x, \quad \delta = -\int y_{d1}\,\Gamma_0'\,w\,\mathrm{d}x \Big/ \int \Gamma_0\,w\,\mathrm{d}x$$

and

$$\beta = 1 + \int u_{b0}\,\Gamma_0\,w\,\mathrm{d}x \Big/ \int \Gamma_0\,w\,\mathrm{d}x$$

are real numbers (because all functions involved in the calculation of γ, δ and β are real). The amplitude equation (58) is similar to the Landau–Ginzburg equation, the only difference being the presence of $\exp(-2\xi)$ in (58). There exist steady solutions, $A = A_s = \pm(\gamma/\delta)^{1/2}$, corresponding to the secondary swirling flows and the trivial solution, $A = 0$. The steady solutions are ξ-independent, but to obtain other solutions, boundary conditions must be formulated.

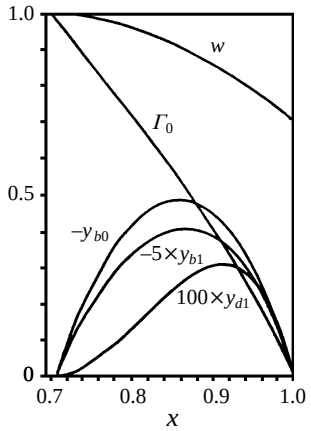

FIGURE 21. The dependence on the polar angle of the stream function of the basic flow (y_{b0}), its changes due to Re (y_{b1}) and due to the nonlinear effect of swirl (y_{d1}). Also the swirl disturbance (Γ_0) and the adjoint solution (w) are shown.

7.2.2. *Boundary conditions for temporal disturbances*

Since the terms with time derivatives in (3) have the coefficient, $\exp(2\xi)$, which is unbounded as $\xi \to \infty$, we need to consider the temporal problem in the spherical layer $r_i \leqslant r \leqslant r_o$. Boundary conditions at $r = r_i$ and $r = r_o$ must be consistent with features of the neutral disturbances. Conical flows and the ξ-independent neutral disturbances satisfy (1b), but the ξ-periodic neutral modes (found in §4.4) do not. To capture this kind of instability and secondary ξ-periodic flows which bifurcate from conical solutions at $Re = Re_{cr}$, we use (1c), i.e. the periodic condition with respect to ξ,

$$f(x, \xi_i) = f(x, \xi_o).$$

Here $\xi_i = \ln r_i$, $\xi_o = \ln r_o$, and $f(x, \xi)$ represents any function related to velocity and pressure. Note that conical flows and the ξ-independent neutral modes satisfy the periodicity condition as well. Therefore, (1c) is more 'soft' than (1b), being relevant for both ξ-independent and ξ-periodic flows. For the ξ-periodic case, $L = r_o - r_i$ must be adjusted to include an integral number of wavelengths. This is not a strong limitation as the range of the similarity region is restricted only by the condition, $L/r_i \quad 1$.

7.2.3. *Small disturbances*

For small disturbances, neglecting the term with A^3 and using the normal-mode representation, $A(T, \xi) = \exp(\lambda T)\, a(\xi)$, reduces (58) to the ordinary differential equation,

$$a_{\xi\xi} - \beta a_\xi + \varepsilon[\gamma - \lambda \exp(2\xi)]\, a = 0, \tag{59a}$$

under uniform boundary conditions

$$a(\xi_i) = a(\xi_o), \quad a_\xi(\xi_i) = a_\xi(\xi_o). \tag{59b}$$

A non-trivial solution necessitates finding an eigenvalue of λ. At $\varepsilon = 0$, the solution, $a = \text{const}$ (e.g. $a = 1$), corresponds to the neutral mode, but λ remains to be determined. To find λ for small ε, we use the expansion, $a = 1 + \varepsilon a_1(\xi) + \ldots$, in (59$a$) and obtain the equation, $a_{1\xi\xi} - \beta a_{1\xi} = \lambda \exp(2\xi) - \gamma$ for terms of $O(\varepsilon)$. If we integrate this equation from ξ_i to ξ_o under conditions (59b), the left-hand side becomes zero and

$$\lambda = 2\gamma(\xi_o - \xi_i)/[\exp(2\xi_o) - \exp(2\xi_i)]. \tag{59c}$$

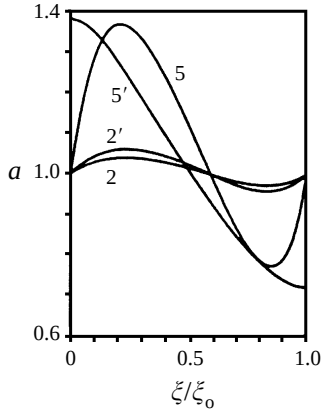

FIGURE 22. The radial distribution of the swirl for small eigenmode disturbances. The numerical (curve 2) and analytical (curve 2′) results at $\xi_0 = 2$. The numerical results at $\xi_0 = 5$ for the periodic (curve 5) and zero-derivative (curve 5′) boundary conditions.

Finally, the solution of (59*a*, *b*) is

$$a = 1 + \varepsilon\{C\exp(\beta\xi) + \lambda\exp(2\xi)/(4-2\beta) + \gamma\xi/\beta\} + O(\varepsilon^2), \tag{59d}$$

where $$C = \{\lambda[\exp(2\xi_o) - 1]/(4-2\beta) + \gamma\xi_o/\beta\}/[1-\exp(\beta\xi_o)].$$

The following numerical results illustrate the approach for typical parameter values.

7.2.4. *Numerical calculation of* γ, δ, *and* β

As an example, consider the temporal problem for swirl bifurcation in a conical meniscus at $x_c = 0.707$ and $\overline{Re}_{cr} = 6.3044$ (figure 13). Figure 21 shows the numerical results for $\psi_{b0} = -y_{b0}$, Γ_0, w, $-5\times y_{b1}$, and $100\times y_{d1}$. Notice that conjugate solution (w) is bounded (this is a check for the calculations) but non-zero at $x = 1$, as distinct from the swirl (Γ_0) and stream function components (y_{b0}, y_{b1}, and y_{d1}) which are zero at $x = 1$. We use the calculated values of the coefficients,

$$\gamma = 0.319, \quad \delta = 0.00997, \quad \beta = -1.204,$$

in the following numerical studies of (58).

Since γ is real and positive, the swirl disturbance grows monotonically with time at each point of the similarity region for $\overline{Re} > \overline{Re}_{cr}$. This growth saturates as the swirl reaches its value corresponding to curve 2 in figure 13. The weakly nonlinear approach (i.e. (58) and the numerical results of γ and δ) yields the saturated amplitude, $A_s = \pm(\gamma/\delta)^{1/2} = \pm 5.66$ or $\Gamma_c = \pm 5.66\,(\overline{Re} - \overline{Re}_{cr})^{1/2}$ (curve 2′ in figure 13), which agrees with the strongly nonlinear results (curve 2). Curves 2 and 2′ in figure 13 are close even for $\overline{Re}$ significantly larger than $\overline{Re}_{cr}$ (e.g. the difference in Γ_c is less than 6% at $\overline{Re} = 20$). This fact reveals that the weakly nonlinear approach is valid in a rather wide range near $\overline{Re} = \overline{Re}_{cr}$.

One further check is the comparison of the present results with those obtained in §5.3.1 for the linear spatial instability. The slope of the curve 3 in figure 13 is $\mathrm{d}\alpha_{00}^{+}/\mathrm{d}\overline{Re} = -0.265$ at $\overline{Re} = \overline{Re}_{cr}$. On the other hand, the slope value is calculated from (58). For steady infinitesimal disturbances, the terms with A_T and A^3 are omitted. Since then the coefficient $\exp(-2\xi)$ can be cancelled, A now depends on 'slow' variable $\varepsilon\xi$ only. Therefore $A_{\xi\xi}$ becomes of $O(\varepsilon^2)$ and so it, too, must be neglected. The reduced form of (58), $\gamma A = \beta A_{\xi}/\varepsilon$, has the normal-mode solution $A = C\exp(\alpha\xi)$ where $\alpha = \varepsilon\alpha_1$ and $\alpha_1 = \mathrm{d}\alpha/\mathrm{d}\overline{Re} = \gamma/\beta = -0.265$ which coincides with the result in §5.3.1.

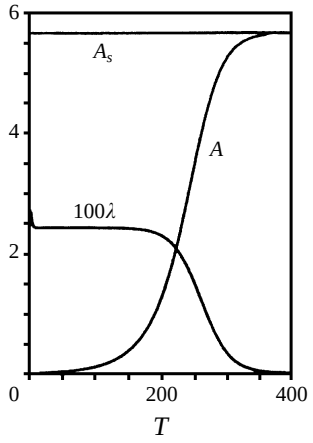

FIGURE 23. Evolution of amplitude A of a swirl disturbance in the supercritical vicinity of Re_{cr} up to saturation at A_s. Curve 100λ shows scaled $\lambda = A^{-1}\mathrm{d}A/\mathrm{d}T$.

7.2.5. *Spatiotemporal evolution*

Take a very small initial disturbance $A(0,\xi)$ and integrate (58) under the boundary conditions,

$$A(T,\xi_i) = A(T,\xi_o), \quad A_\xi(T,\xi_i) = A_\xi(T,\xi_o).$$

First, the disturbance develops into the growing normal mode, $A(T,\xi) = C\exp(\lambda T)\,a(\xi)$, as other modes are decaying. It appears that (59*c*, *d*) provide valid λ and a even where ε is not very small. For example, (59*c*) yields $\lambda = 0.0238$ at $\xi_i = 0$ and $\xi_o = 2$, while calculation of (59*a*, *b*) at $\varepsilon = 1$ gives $\lambda = 0.0243$. Also, $a(\xi)$ at $\varepsilon = 1$ is close to $1+\varepsilon a_1(\xi)$ with $\max|a(\xi)-1| < 0.05$. Figure 22 shows $\alpha(\xi)$ obtained by the numerical calculation (curve 2) and from (59*d*) (curve 2′) at $\varepsilon = 1$ and $\xi_o = 2$.

Taking into account that (*a*) amplitude $A(T,\xi)$ of the growing mode is ξ-independent at $\varepsilon = 0$, (*b*) the same A depends weakly on ξ even at $\varepsilon = 1$ and (*c*) the saturation amplitude $A_s = (\gamma/\delta)^{1/2}$ is ξ-independent, consider an approximation of (58), neglecting $A_{\xi\xi}$ and A_ξ. Then introducing of the new variable, $\bar{T} = T\exp(2\xi) = \varepsilon\nu t/r^2$, reduces (58) to the Landau equation, $A_{\bar{T}} = \gamma A - \delta A^3$, with the solution,

$$A = A_s[1 + C\exp(-2\gamma\bar{T})]^{-1/2}, \tag{60}$$

where the integration constant C is defined by an initial amplitude $A(0)$, $C = (\gamma/\delta)\,A^{-2}(0) - 1$. According to (60), the saturation of A to A_s occurs first near $r = r_i$, and then near $r = r_o$. This feature is consistent with the numerical results for $a(\xi)$ whose maximum and minimum values are located near $r = r_i$, and $r = r_o$, respectively (figure 22). The extrema become more prominent for large ξ_o as curve 5 in figure 22 shows at $\varepsilon = 1$ and $\xi_o = 5$. As ξ_o increases, boundary layers develop near $r = r_i$, and $r = r_o$. The boundary layers arise from the periodic conditions which strongly affect $a(\xi)$ near the boundaries. For comparison, we have calculated $\alpha(\xi)$ at the same parameters as those for curve 5 but under the conditions, $a_\xi(\xi_i) = a_\xi(\xi_o) = 0$ which follow from (1*b*) (curve 5′ in figure 22). The boundary layers disappear for the periodic conditions as well, as $A(T,\xi)$ saturates at A_s.

Consider an example of the transition process from basic to secondary steady solutions. To this end, integrate (58) using the first-order implicit numerical scheme with respect to time.

$$A_n - A_{n-1} = \Delta\exp(-2\xi)[\gamma A_n - \delta A_n^3 + (A_{n\xi\xi} - \beta A_{n\xi})/\varepsilon], \tag{61}$$

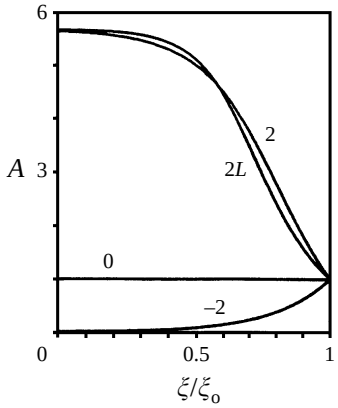

FIGURE 24. The radial distribution of the saturated swirl given at $\xi = \xi_0$ for $Re_{cr} + \varepsilon$ with $\varepsilon = -2, 0, 2$ (shown near the curves) compared with the solution of the Landau equation (curve $2L$).

where $\Delta = T_n - T_{n-1}$. At $T = T_0 = 0$, the uniform initial distribution, $A_0 = 0.01$, is chosen. At each $n = 1, 2, \ldots$, integration of (61) with respect to ξ yields $A_n(\xi)$. To satisfy the periodic condition, we apply the Newton shooting procedure. Curve A in figure 23 shows the results for $A(T, \xi_o)$ at $\varepsilon = 1$ and $\xi_o = 2$ (shown only for $\xi = \xi_0$, because $A(T, \xi)$ is found to be nearly ξ-independent in this case). Curve 100λ (scaled $\lambda = \mathrm{d} \ln A / \mathrm{d}T$) displays the exponential stage of the transition. For small T, λ strongly varies (until $A(T, \xi)$ transforms from $A_0(\xi)$ to the growing normal mode) saturating at $\lambda = 0.0243$. This 'pre-exponential' linear development is not universal; it depends on the initial distribution $A_0(\xi)$. For $40 < T < 170$, $A(T, \xi) \approx C \exp(\lambda T)\, a(\xi)$ with $a(\xi)$ shown by curve 2 in figure 22 and $\lambda \approx \text{const} = 0.0243$. This exponential linear stage is universal; the character of $A_0(\xi)$ affects only C. For larger T (when A exceeds 1 in figure 23), the nonlinear term in (58) suppresses the exponential growth and causes the saturation of $A(T, \xi)$ at A_s (the horizontal line in figure 23). Similar time evolution, i.e. the monotonic growth of the amplitude, occurs at each fixed observation point (r, θ, ϕ) of the flow region, and, therefore, the temporal instability is not convective in this case.

7.2.6. *Fixed circulation at $r = r_o$*

In practical flows, circulation can be forced to be small at $r = r_o$. For example, the no-slip condition makes circulation zero on the copper wall in the experiment by Bojarevics *et al.* (1989) and on the capillary tube in electrosprays (see §§1.2 and 5.4). Some micro-vanes or small asymmetry of the walls can induce a weak swirl which spreads and accumulates in the similarity region for $\overline{Re} > \overline{Re}_{cr}$. While the swirl can become strong near $r = r_i$, the no-slip condition keeps circulation small near the walls, i.e. at $r = r_o$. To model this effect, integrate (58) under the following conditions: $A(T, \xi_o) = A_o$ fixes the swirl (e.g. by a small value) at $r = r_o$; $A_\xi(T, \xi_i) = 0$ allows circulation to be saturated and large near $r = r_i$. Our calculations have revealed that time evolution is similar to that shown in figure 23, differing only by the fact that saturated amplitude $A_s = A(\infty, \xi)$ is now ξ-dependent. While there are no new interesting effects related to time evolution, the striking character of $A_s(\xi)$ is important for understanding of the swirl accumulation mechanism. Since A_s is governed by (58) with $A_T = 0$, the coefficient $\exp(-2\xi)$ can be cancelled, and thus the problem reduces to

$$A_{\xi\xi} - \beta A_\xi + \varepsilon(\gamma A - \delta A^3) = 0, \quad A_\xi(\xi_i) = 0, \quad A(\xi_o) = A_o.$$

Figure 24 shows the numerical results for $\varepsilon = -2$, 0 and 2 (see the figures near the curves) at $\xi_i = 0$, $\xi_o = 10$ and $A_o = 1$, as well as the analytical result (curve $2L$, $\varepsilon = 2$), which corresponds to the limiting case, $\varepsilon \to 0$. In this case, A depends on 'slow' variable $\varepsilon\xi$ only; hence $A_{\xi\xi}$ becomes of $O(\varepsilon^2)$ now and must be neglected. As a result, (58) reduces to the Landau equation, $A_{\bar{T}} = \gamma A - \delta A^3$, having solution (60) where now $\bar{T} = \varepsilon(\xi - \xi_o)/\beta$. Note that curves 2 and $2L$ do not differ markedly, although $\varepsilon = 2$ is not too small.

Since $Re = Re_{cr} + \varepsilon$, curves -2, 0 and 2 illustrate the swirl distribution for the subcritical, critical and supercritical values of Re. Although the swirl is forced to the non-zero value, $A_o = 1$, at the outer boundary of the similarity region, A rapidly decays as r decreases at $Re = Re_{cr} - 2$. Therefore no swirl is observed in the experiments for $Re < Re_{cr}$. At $Re = Re_{cr}$, the swirl does not decay inward into the region but remains small, provided that the outer source of circulation is weak. At $Re = Re_{cr} + 2$, the swirl grows rapidly as r decreases until saturation at $A_s = (\gamma/\delta)^{1/2}$. Note that the saturation value A_s does not depend on A_o and can be significantly larger than A_o as figure 24 illustrates. Therefore the swirl can be easily observed in the experiments for $Re > Re_{\mathrm{cr}}$.

The above spatiotemporal analysis of swirl development, together with the linear spatial instability and bifurcation studies, provides a clear and complete explanation of the intriguing phenomenon of the appearance of swirl in initially swirl-free flows.

7.3. *Temporal instability near the fold bifurcation*

For the two solution branches near a fold, the general theory (Iooss & Joseph 1981) states that at least one of the branches corresponds to the unstable solution. Determining which branch is unstable requires stability analysis for each specific case. The spatial stability analysis in §4.3 addresses this issue for folds in swirl-free jets. Here the temporal instability is studied for the same flows using an approach similar to that in §7.2. However, the present problem differs from that in §7.2 in two ways. The first is fundamental resulting from the difference in the character of bifurcation: the derived amplitude equation involves a quadratic (but not cubic as in §7.2) term with respect to amplitude A. The second is technical: the number of involved equations is larger here than that in §7.2, which makes calculations more laborious.

7.3.1. *Amplitude equation*

To derive the amplitude equation, we start from the system,

$$y_x = u + u_\xi, \tag{62a}$$

$$(1-x^2)\,u_{xx} = (2x-y)\,u_x - u_{\xi\xi} - u_\xi - uu_\xi - u^2 - 2q + q_\xi - y^2/(1-x^2) + u_\tau \exp(2\xi), \tag{62b}$$

$$(1-x^2)\,q_x = (1-x^2)\,(u_x - u_{x\xi}) + uy_\xi - yu_\xi - yu + y_\xi - y_{\xi\xi} - xy^2/(1-x^2) + y_\tau \exp(2\xi), \tag{62c}$$

$$J_x = x[u^2 + 2u + q - 2u_\xi] - yu - 2y + y\xi - (1-x^2)\,u_x, \tag{62d}$$

which follows from (3) for axisymmetric swirl-free flows and from (11) with $J_x = j$. In the vicinity $Re = Re_{cr} + \varepsilon$ of a fold point (e.g. F_1 in figure 5), we use the expansion,

$$y = y_{b0} + \varepsilon y_{b1} + \varepsilon A(\varepsilon\tau, f(\xi,\varepsilon))\,y_{d0}(x) + \varepsilon^2 A_2(\varepsilon\tau, f(\xi,\varepsilon))\,y_{d1}(x) + \dots, \tag{63}$$

(using similar representations for u, q, and J). Note that, as distinct from (54), the expansion for disturbances in (63) begins with the terms of $O(\varepsilon)$. This is because the disturbances involved in the transition process are of the same order of magnitude as the difference between two steady solutions (at a fixed J_1) near the fold point. This difference is $O(|J_1 - J_{1cr}|^{1/2})$ as figure 5 shows for folds F_1 and F_2. Since $J_2 - J_{1cr} \sim$

$(Re-Re_{cr})^2$ near these folds, the switching disturbances are $O(\varepsilon)$ in the leading order of magnitude.

The boundary conditions for disturbances are

$$y_d = J_d = 0 \quad \text{at} \quad x = x_c, \quad y_d = J_d = 0, \quad q_d + u_{b0}\, u_d - u_d' = 0 \quad \text{at} \quad x = 1. \tag{64}$$

Introduce $\boldsymbol{U} = \{y, u, q, J\}$. In the $O(\varepsilon)$ order, (62) and (63) yields the system for $\boldsymbol{U}_{d0}$,

$$L_1(\boldsymbol{U}_{d0}) \equiv y' - u = 0, \tag{65a}$$

$$L_2(\boldsymbol{U}_{d0}) \equiv (1-x^2)\, u'' - (2x - y_{b0})\, u' + y u_{b0}' + 2q + 2u_{b0}\, u + 2y_{b0}\, y/(1-x^2) = 0, \tag{65b}$$

$$L_3(\boldsymbol{U}_{d0}) \equiv (1-x^2)\, q' - (1-x^2)\, u' + y_{b0}\, u + y u_{b0} + 2x y_{b0}\, y/(1-x^2) = 0, \tag{65c}$$

$$L_4(\boldsymbol{U}_{d0}) \equiv J' - x(2u_{b0}\, u + 2u + q) + 2y + y_{b0}\, u + y u_{b0} + (1-x^2)\, u'] = 0, \tag{65d}$$

where the subscript $d0$ is omitted for y, u, q and J. Equations (65*a–c*) coincide with (30*a–c*), and (65*d*) coincides with (12) at $\alpha = 0$. The problem (64)–(65) has a non-trivial solution at $Re = Re_{cr}$, which corresponds to the neutral mode.

Equations for disturbances in the $O(\varepsilon^2)$ order are

$$A_2\, L_1(\boldsymbol{U}_{d1}) = \varepsilon^{-1} A_\xi\, u, \tag{66a}$$

$$\begin{aligned} A_2\, L_2(\boldsymbol{U}_{d1}) = &- A[y_{b1}\, u' + y u_{b1}' + 2u_{b1}\, u + 2y_{b1}\, y/(1-x^2)] - A^2[y u' + u^2 + y^2/(1-x^2)] \\ &+ \varepsilon^{-1} A_\xi[(u_{b0} - 1)\, u + q] - \varepsilon^{-1} A_{\xi\xi}\, u + A_\tau\, u \exp(2\xi), \end{aligned} \tag{66b}$$

$$\begin{aligned} A_2\, L_3(\boldsymbol{U}_{d1}) = &- A[y_{b1}\, u + y u_{b1} + 2x y_{b1}\, y/(1-x^2)] - A^2[y u + x y^2/(1-x^2)] \\ &+ \varepsilon^{-1} A_\xi[(1 + u_{b0})\, y - y_{b0}\, u - (1-x^2)\, u_x] - \varepsilon^{-1} A_{\xi\xi}\, y + A_\tau\, y \exp(2\xi), \end{aligned} \tag{66c}$$

$$A_2\, L_4(\boldsymbol{U}_{d1}) = A[2x u_{b1}\, u - y_{b1}\, u - y u_{b1}] + A^2[x u^2 - y u] + \varepsilon^{-1} A_\xi[y - 2x u], \tag{66d}$$

where the subscript $d1$ is omitted for y, u, q and J in the right-hand sides. Again, A_ξ and $A_{\xi\xi}$ are magnitudes of $O(\varepsilon)$, so that all terms in (66) are of the same order.

Since the uniform version of (66) coincides with (65) and has the non-trivial solution $\boldsymbol{U}_{d1} = \boldsymbol{U}_{d0}$, the right-hand side of (66) must satisfy the orthogonality condition. We obtain the adjoint solution $\boldsymbol{W}$ by integration of the problem described in the Appendix (note that (A 9) reduces to the fifth-order system at $m = \alpha = 0$ and $\Gamma_b = \Gamma_d \equiv 0$). If we take the scalar product of (66) with $\boldsymbol{W}$ (which includes integration with respect to x from $x = x_c$ to $x = 1$), the left-hand side becomes zero and the right-hand side becomes x-independent. The resulting equation for amplitude,

$$A_T = \exp(-2\xi)[\gamma A - \delta A^2 + (A_{\xi\xi} - \beta A_\xi)/\varepsilon], \tag{67}$$

is similar to (58) except for δA^2 which replaces δA^3 in (58). Therefore, the results of §7.2.3, where the nonlinear term is neglected, apply to (67) as well. Now calculate coefficients γ, δ and β for a particular fold problem.

7.3.2. *The Squire jet*

The simplest case which allows analytical solutions is the fold point for the Squire jet at $x_c = 0$ and $Re = 0$ (§4.3.2). Analytical solutions (31) exist for y_{d0}, u_{d0}, and q_{d0}. Also (32) yields $J_{d0} = 2x(1-x^2)$. The adjoint solution is governed by the equations,

$$w_5 = 1, \quad w_1' = 2, \quad w_2' = -w_1 - 2x, \quad w_3' = 1 - x^2 - w_2 - 2x w_3/(1-x^2) - w_4,$$
$$w_4' = 2w_3/(1-x^2) - x.$$

Analysis yields the solutions $w_1 = 2x - 2$ and $w_2 = 2x - 2x^2$, while w_3 and w_4 are found numerically and shown in figure 25. The above analytical solutions help us to check numerical results.

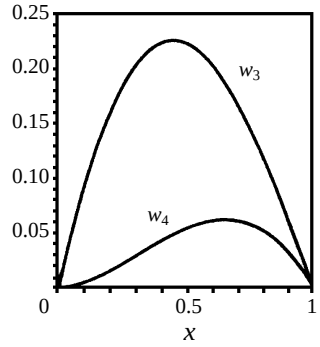

FIGURE 25. Components w_3 and w_4 of the adjoint solution for the Squire jet at $x_c = 0$ and $Re = 0$.

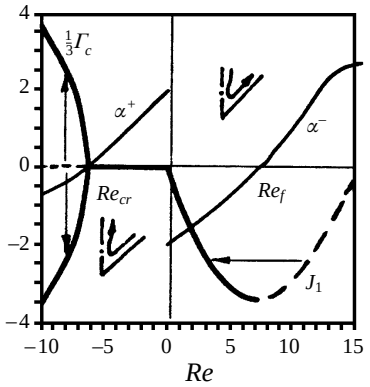

FIGURE 26. Swirl (curve $\frac{1}{3}\Gamma_c$) and fold (curve J_1) bifurcation in the Squire jet at $x_c = 0.707$. Curves α^+ and α^- show the leading eigenvalues. The broken curves show unstable solutions, and arrows show transitions between unstable and stable steady states. The insets show flow schematics.

The calculations give $\gamma > 0$, $\delta < 0$ and $\beta > 0$ along fold F_1 in figure 6. Note that $\gamma > 0$ means the temporal instability of solutions corresponding to the intermediate branch connecting F_1 and F_2 for $x_c < 0$ (e.g. see figure 5*b*) and the upper branch for $x_c > 0$ (figure 5*c*). At $x_c = 0$, the converging-near-plane flow ($Re < 0$) is found stable near the fold. There is a transition process switching between the diverging and converging steady states at a fixed flow force J_1. A disturbance of the diverging flow develops from a small initial amplitude $A_0(\xi)$ and saturates at the steady state $A_s = \gamma/\delta$ corresponding to the converging flow. Negative γ/δ means that Re decreases during this transition since the diverging flow corresponds to larger Re than that for the converging flow at the same J_1.

Exploiting the feature that A is nearly ξ-independent for small ε (§7.2.3), consider (as in §7.2.5) an approximation where $A_{\xi\xi}$ and A_ξ are neglected in (67). Then introducing of the new variable, $\bar{T} = T\exp(2\xi) = \varepsilon\nu t/r^2$, reduces (67) to $A_{\bar{T}} = \gamma A - \delta A^2$, with the solution,

$$A = A_s[1 + (A_s/A_0 - 1)\exp(-\gamma\bar{T})]^{-1}, \tag{68}$$

where A_0 is an initial value of amplitude at $T = 0$. Note that the transition to the diverging flow occurs for $A_0 < 0$, $A_0/A_s < 1$. For $A_0 > 0$, A becomes infinite as a finite $\bar{T}$ corresponding to (68); note, however, that the weakly nonlinear approach is invalid for very large $|A|$.

Figure 26 shows the cumulative illustration of the §7 results for the swirl and fold bifurcations in the flow inside the cone with $x_c = 0.707$; the insets show flow schematics for $Re < 0$ (left) and for $Re > 0$ (right). Curve $\frac{1}{3}\Gamma_c$ shows the pitchfork bifurcation of swirl, and curve α^+ shows the leading spatial eigenvalue as Re decreases from 0. The instability of the basic flow (shown by the broken line for $Re < Re_{cr} = -6.3$) occurs owing to outer disturbances since α is positive at $Re = 0$ and becomes negative for $Re < Re_{cr}$. The vertical arrows depict the transitions between the steady states at a fixed Re.

Curve J_1 shows the fold bifurcation (corresponding to the minimum of $J_1 = -3.4$ at $Re = Re_f = 7.2$) and curve α^- shows the leading α as Re increases from 0. The horizontal arrow shows the transition between the unstable (for $Re > Re_f$) and stable (for $Re < Re_f$) steady states for a fixed J_1. Since α is negative at $Re = 0$ and becomes positive for $Re > Re_f$, the switching disturbances are inner. For both the swirl and fold bifurcations, the spatial and temporal instabilities occur in the same range ($Re < Re_{cr}$ and $Re > Re_f$) of the Reynolds number. In the supercritical vicinities of bifurcations studies in §§7.2 and 7.3, the transition from the basic to secondary steady flows is time-monotonic and occurs at any fixed observation point inside the similarity region.

8. Discussion and concluding remarks

Here we discuss the main points of our approach and comment on possible future extensions.

8.1. *Inner and outer modes*

The classification of disturbances into inner and outer plays a crucial role in our stability analysis since it helps in the identification of the origin of disturbances responsible for the instability. An interpretation of different modes of spatially developing disturbances has been a key problem starting from the pioneering works by Dean (1934) for the Jeffery–Hamel flow and Gaster (1962) for parallel flows.

Since NSEs are parabolic with respect to time but elliptic with respect to spatial coordinates, there is a strong difference in the spectrum of eigenvalues λ for temporally, $\sim \exp(\lambda t)$, and spatially, $\sim \exp(\alpha\xi)$, developing disturbances. In the temporal case, there is no eigenvalue with $\lambda_r > 0$ for stable flows. In contrast, the number of eigenvalues having both signs of α_r is infinite in the spatial case, independent of whether a flow is stable or unstable. The spectrum varies with Re, and one of the eigenvalues crosses the $\alpha_r = 0$ line on the neutral curve. A careful analysis is needed to find which spatial modes correspond to the instability, and what their physical meaning may be.

For this reason, the identification of the spatial instability is more sophisticated than that for the temporal instability (Huerre & Monkewitz 1990). Prior studies have discarded some spatial modes as 'spurious' or 'irrelevant'; this paper provides better understanding of the role and physical meaning of all spatial modes in conical flows. For a proper identification, we first consider a fluid at rest. Its stability is physically obvious, helping to clarify the role of different modes.

The term 'propagating downstream or upstream' might be confusing for disturbances in the conical flows we have studied. Consider, for example, the flow patterns shown in figure 14(*b*) or the insets in figure 26. For a fixed r, there are inflows and outflows depending on θ, and the maximum velocities of the inflow and outflow are of the same order of magnitude. For example, the swirl bifurcation in figure 26 occurs at $Re = Re_{cr} = -6.3$ characterizing the maximum inflow velocity (on the cone surface) with $Re_a = 7.6$ characterizing the maximum outflow velocity (on the axis). For

the fold bifurcation in the same figure, $Re = Re_f = 7.2$ and $Re_a = -6.1$. The growing disturbances are not localized in the inflow or outflow region but are of the same order of magnitude in the entire range of the polar angle, $0 \leqslant \theta \leqslant \theta_c$. Therefore the disturbances cannot – and quite possibly should not – be characterized as propagating 'upstream' or 'downstream'. In contrast, the fact that the disturbances originate at the inner and outer boundaries of a similarity region follows directly from the analysis at $Re = 0$.

By gradually increasing Re, we identify the instability as inner or outer depending on how $\alpha_r(Re)$ crosses zero, which clearly indicates that the corresponding disturbances originate either at the inner or at the outer boundaries. For specific conical flows studied here, there exist examples of instability caused by both inner and outer disturbances. In particular, an outer disturbance causes the swirl bifurcation at $Re = Re_{cr}$, and an inner disturbance causes the fold bifurcation at $Re = Re_f$ in figure 26.

We have also shown what occurs when the inner and outer spectral branches merge, resulting in global modes. The global disturbances are responsible for the spatially oscillatory instability (§4.4) which leads to the secondary steady regimes periodic with respect to $\ln r$. Thus, the classification of disturbances into inner and outer allows us to study a variety of physically different problems using the common approach.

8.2. *The role of similarity*

Azimuthal symmetry breaking, formation of swirl, radial spatial oscillations, and hysteresis in conical swirl-free flows are among the bifurcation phenomena captured by our stability approach which reveals the origin of disturbances responsible for these metamorphoses. There are also problems such as the azimuthal symmetry breaking and hysteresis in swirling flows, which are not included here. The approach used here can be extended in a straightforward manner to a variety of heat transfer, scalar diffusion, and magnetohydrodynamic problems, e.g. conical flows involving the onset of thermal convection, hydromagnetic dynamo, and Marangoni convection due to surfactants. This rather wide range of applications results from conical similarity allowed by all equations governing the above mentioned problems.

Although conical flows are strongly non-parallel, the linear stability problem is exactly reduced to ODEs because our approach effectively exploits the similarity of basic flows. A special transformation of dependent and independent variables extends the similarity advantages to non-similar disturbances. Govindarajan & Narasimha (1995) have developed a similar technique using similarity variables for the stability study of Falkner–Skan flows, enabling them to take into account non-parallel effects more precisely. Since the Falkner–Skan similarity is a feature of the boundary layer equations but not of NSEs, that approach is approximate, in contrast to the present paper where the reduction, suitable for any conical flow, is exact – an important difference, which, however, disappears for unsteady disturbances.

8.3. *Unsteadiness*

If one keeps the unsteady terms in NSEs, then terms like $\exp(2\xi)\, u_\tau$ are present in (3). Since coefficients become dependent on ξ, the normal form (5) with respect to ξ cannot be applied. This makes the temporal stability study significantly more difficult than that for steady disturbances – a difficulty which is overcome here with the help of a small parameter expansion in the vicinity of $Re = Re_{cr}$ for the instabilities found. The temporal evolution is slow for $Re = Re_{cr} + \varepsilon$ and this fact allows the weakly unsteady approach which includes also weakly nonlinear effects. Such a small parameter technique is developed in §7 where the nonlinear amplitude equations of the

Landau–Ginzburg type are deduced describing the spatiotemporal dynamics of the leading disturbances. The detailed analysis in the cases of the swirl and fold bifurcations reveals that the switching disturbances grow monotonically with time until saturation, causing the transition from the primary to secondary steady flow for $Re > Re_{cr}$. These disturbances do not reveal a wavelike character, but grow with time at any fixed observation point of the similarity region (e.g. see figures 24 and 25), and, therefore, the instability is absolute (Huerre & Monkewitz 1990).

We expect similar results for most of the cases considered here. The exceptions would be the vicinities of the triple (§4.4.3) and intersection (§6.3) points of neutral curves. Owing to the multiple instability, the established secondary flows may exhibit complex (chaotic?) spatiotemporal behaviour in these vicinities. This requires further study, including a multi-mode nonlinear stability analysis.

The small parameter technique allows the temporal instability studies only near $Re = Re_{cr}$. Another way to study unsteady disturbances approximately is the so-called local approach. In terms such as $\exp(2\xi)\, u_\tau$, the time derivative is not treated as a small quantity, but ξ is 'frozen' as a fixed value ξ_0. This approximation is similar to the quasi-parallel approach in the stability study of boundary-layer flows. For example, it is valid if a longitudinal lengthscale of disturbances, say wavelength, is small compared with the distance from the jet origin. For such an approach, advanced methods of the stability theory for quasi-parallel flows can be used.

9. Summary of new results

1. A special form of the Navier–Stokes equations is deduced. For steady flows, its coefficients depend on a single variable, the polar angle. This drastically eases the analysis of steady-state bifurcations and instabilities occurring in conical flows. In particular, the linear stability problem with respect to steady three-dimensional disturbances is reduced exactly to an ODE system despite the fact that most conical flows are strongly non-parallel.

2. A variety of analytical solutions are found for disturbances in a still fluid in the full and half-space under the no-slip, stress-free and momentum-free boundary conditions.

3. Physical interpretation of the above solutions leads to classification of disturbances into 'inner' and 'outer'. There is a similarity region, $r_i < r < r_o\,(r_o/r_i \gg 1)$, for conical flows, and the inner (or outer) disturbances are those originating at $r = r_i$ (or r_o). Merging of the inner and outer modes generates 'global' disturbances.

4. Hysteretic transitions are found in swirl-free jets resulting from a point source of the axial momentum, J_1, in the conical region, $\theta < \theta_c$. A cusp and two curves of the fold catastrophes are found on the parameter plane (J_1, θ_c). The instability related to the folds corresponds to the inner (outer) disturbances for $\theta_c < (>)\,90°$. A new kind of axisymmetric instability is found (caused by global disturbances), which leads to the secondary steady flows oscillating in the radial direction.

5. The appearance of swirl in the swirl-free flows springs from outer disturbances. This statement is valid for single-phase and two-phase flows in electrosprays driven by surface shear stresses and for a converging-near-surface flow driven by electromagnetic body forces.

6. Azimuthal symmetry breaking is caused by inner disturbances in the Squire–Wang, Marangoni, and diverging-near-surface electro-vortex and thermal-convection flows. The inner-mode nature of the azimuthal instability does not depend on the type of flow forcing or on conditions at remote boundaries.

7. We derive nonlinear amplitude equations of the Landau–Ginzburg type, which describe the spatiotemporal dynamics of disturbances near $Re = Re_{cr}$. Our analysis of the amplitude equations for the swirl and fold bifurcations reveals that disturbances monotonically grow with time at each fixed point of the similarity region and saturate at the secondary steady solution in the supercritical vicinity of $Re = Re_{cr}$.

The authors dedicate this paper to the memory of Michael Goldshtik. This research has been supported by the US National Science Foundation grant CTS-9622302. We cordially thank Dr H. C. Kuhlmann for providing the reference Thompson (1855), and a copy of the paper.

Appendix. Adjoint problem

Rewrite (6) as a system of the first-order differential equations $u_k' = L_{kl}\,u_l$ (where $k, l = 1, \ldots, 6$ and the right-hand side is a sum with respect to l). The components, u_l, u_k' and L_{kl}, are:

	$u_1 = y_d$	$u_2 = u_d$	$u_3 = u_d'$	$u_4 = \Gamma_d$	$u_5 = \Gamma_d'$	$u_6 = q_d$
$u_1' = y_d'$	—	$(1+\alpha)$	—	$-m\Gamma_d p_x$	—	—
$u_2' = u_d'$	—	—	1	—	—	—
$u_3' = u_d''$	$-u_b' p_x - 2y_b p_x^2$	$[(\alpha-2)u_b + p_b]p_x$	$(2x - y_b)p_x$	$-2\mathrm{i}\Gamma_b p_x^2$	—	$(\alpha-2)p_x$
$u_4' = \Gamma_d'$	—	—	—	—	1	—
$u_5' = \Gamma_d''$	$(i\Gamma_b - p_2)p_x$	$-2mp_x$	—	$(\alpha u_b + p_5)p_x$	$-y_b p_x$	mp_x
$u_6' = q_d'$	$p_7 p_x - 2xy_b p_x^2$	$-(1+\alpha)y_b p_x$	$(1-\alpha)$	$p_3 p_x - 2\mathrm{i}x\Gamma_b p_x^2$	mp_x	—

(A 1)

where $p_x = 1/(1-x^2)$, $p_6 = p_1 - \alpha - \alpha^2$, $p_7 = p_5 - (1-\alpha)u_b$. The components of L_{kl} appear in (A 1). Similar tables are used for other systems below.

The adjoint system is $w_k' = L_{kl}^a w_1$, where $L_{kl}^a = -L_{lk}^c$ and subscript c means complex conjugate. The components of the adjoint system are:

	w_1	w_2	w_3	w_4	w_5	w_6
w_1'	—	—	$u_b' p_x + 2y_b p_x^2$	—	$(\mathrm{i}\Gamma_b - p_2)p_x$	$2xy_b p_x^2 - p_7^c p_x$
w_2'	$-(1+\alpha^c)$	—	$-[(\alpha-2)u_b + p_6^c]p_x$	—	$2mp_x$	$(1+\alpha^c)y_b p_x$
w_3'	—	-1	$-(2x - y_b)p_x$	—	—	$-(1-\alpha^c)$
w_4'	$m\Gamma_d p_x$	—	$-2\mathrm{i}\Gamma_b p_x^2$	—	$-(\alpha^c u_b + p_5^c)p_x$	$-p_3 p_x - 2\mathrm{i}x\Gamma_b p_x^2$
w_5'		—	—	-1	$y_b p_x$	$-mp_x$
w_6'		—	$-(\alpha^c - 2)p_x$	—	$-mp_x$	—

(A 2)

Boundary conditions for $\boldsymbol{W}$ follow from the requirement

$$u_l\,w_l = 0 \quad \text{at} \quad x = 1, \quad x = x_c. \tag{A 3}$$

For U bounded at $x = 1$, (7b) reduces (A 3) to

$$w_2\,u_d + w_3\,u_d' + w_5\,\Gamma_d' + w_6\,q_d = 0. \tag{A 4}$$

Then at $m \neq 0$, (7c) reduces (A 4) to $w_3\,u_d' + w_5\,\Gamma_d' + w_6\,q_d = 0$. To satisfy this for arbitrary values of $u_d'(1)$, $\Gamma_d'(1)$ and $q_d(1)$, the conditions for $\boldsymbol{W}$ are

$$w_3(1) = w_5(1) = w_6(1) = 0 \quad \text{at} \quad m \neq 0. \tag{A 5a}$$

At $m = 0$, (A 4) and (7*c*) yield

$$\left.\begin{aligned} &2w_2(1) = [(\alpha-2)\,u_b(1)-\alpha-\alpha^2]\,w_3(1), \quad w_5(1) = 0, \\ &2w_6(1) = (\alpha-2)\,w_3(1) \quad \text{at} \quad m = 0. \end{aligned}\right\} \tag{A 5b}$$

Because of the no-slip condition (8*b*) and (A 3).

$$w_3 = w_5 = w_6 = 0 \quad \text{at} \quad x = x_c. \tag{A 6}$$

The stress-free condition (10*b*) corresponds to

$$w_2 = w_6 = 0, \quad 2xw_5-(1-x^2)\,w_4 = 0 \quad \text{at} \quad x = x_c. \tag{A 7}$$

The flow-force-free condition for disturbances (see §2.4.4) needs special treatment as follows: Extent $\boldsymbol{U}$ up to seven components by putting $u_7 = J_d$ where J_d is defined by (12) with integration from $x = x_c$ to x. Then (A 1) transforms to

	u_1	u_2	u_3	u_4	u_5	u_6
u_1'	—	$(1-\alpha)$	—	$-m\Gamma_d p_x$	—	—
u_2'	—	—	1	—	—	—
u_3'	$-u_b' p_x-2y_b p_x^2$	$[(\alpha-2)\,u_b+p_6]p_x$	$(2x-y_b)p_x$	$-2\mathrm{i}\Gamma_b p_x^2$	—	$(\alpha-2)\,p_x$
u_4'	—	—	—	—	1	—
u_5'	$(\mathrm{i}\Gamma_b-p_2)\,p_x$	$-2mp_x$	—	$(\alpha u_b+p_5)\,p_x$	$-y_b p_x$	mp_x
u_6'	$p_7 p_x-2xy_b p_x^2$	$-(1+\alpha)\,y_b p_x$	$(1-\alpha)$	$p_3 p_x-2\mathrm{i}x\Gamma_b p_x^2$	mp_x	—
u_7'	$\alpha-2-u_b$	$2x(1-\alpha+u_b)-y_b$	$-(1-x^2)$	—	—	x

(A 8)

and (A 2) transforms to

	w_1	w_2	w_3	w_4	w_5	w_6	w_7
w_1'	—	—	$u'_b p_x+2y_b p_x^2$	—	$(\mathrm{i}\Gamma_b+p_2)\,p_x$	$2xy_b p_x^2-p_T^c p_x$	$2+u_b-\alpha$
w_2'	$-(1+\alpha)$	—	$-[(\alpha-2)\,u_b+p_6^c]p_x$	—	$2mp_x$	$(1+\alpha)\,y_b$	$y_b-2x(1-\alpha+u_b)$
w_3'	—	-1	$-(2x-y_b)\,p_x$	—	—	$-(1-\alpha)$	$(1-x^2)$
w_4'	$m\Gamma_d p_x$	—	$-2\mathrm{i}\Gamma_b p_x^2$	—	$-(\alpha u_b+p_5^c)\,p_x$	$-p_3 p_x-2\mathrm{i}x\Gamma_b p_x^2$	—
w_5'	—	—	—	-1	$y_b p_x$	$-m\Gamma'_d p_x$	—
w_6'	—	—	$-(\alpha-2)\,p_x$	—	$-mp_x$	—	$-x$
w_7'	—	—	—	—	—	—	—

(A 9)

The last equation of the adjoint problem is $w_7' = 0$; i.e. w_7 is a constant. This constant cannot be found from the boundary conditions for $\boldsymbol{W}$ because (A 3) does not involve w_7 ($u_7 = 0$ at $x = 1$ and $x = x_c$ according to (12)). At $x = 1$, (A 5) remains valid, but now there are four conditions,

$$w_2 = w_3 = w_6 = 0, \quad (1-x^2)\,w_4+2xw_5 = 0 \quad \text{at} \quad x = x_c, \tag{A 10}$$

which follow from (A 3) and the conditions for $\boldsymbol{U}$ in §2.4.4.

If integration runs from $x = x_c$ to $x = 1$, then one can begin by guessing $w_1(x_c)$, $w_5(x_c)$ and w_7 while (A 10) specifies the others $w_k(x_c)$. The guessed quantities have to be adjusted to satisfy (A 6). To avoid the trivial solution, $\boldsymbol{W} = 0$, one of the guessed parameters can be chosen as 1 (e.g. $w_7 = 1$). Then to satisfy all conditions (A 6), α has to be found as eigenvalue. The problems for $\boldsymbol{U}$ and $\boldsymbol{W}$ must have the same eigenvalues α. This feature serves as a check of calculations.

REFERENCES

Ardalan, K., Draper, K. & Foster, M. R. 1995 Instability of type I Long's vortex at large flow force. *Phys. Fluids* **7**, 365–373.

Banks, W. H. H., Drazin, P. G. & Zaturska, M. A. 1988 On perturbations of Jeffery–Hamel flow. *J. Fluid Mech.* **186**, 559–581.

Batchelor, G. K. 1967 *An Introduction to Fluid Dynamics*. Cambridge University Press.

Beran, P. S. & Culick, F. E. C. 1992 The role of non-uniqueness in the development of vortex breakdown in tubes. *J. Fluid Mech.* **242**, 491–527.

Bertolotti, F. P. 1995 Analysis of the birth and evolution of disturbances in three-dimensional boundary layer, using the parabolized stability equations. *Proc. IUTAM Symp., Manchester*, pp. 17–20, 1995.

Bojarevics, V., Freibergs, J. A., Shilova, E. I. & Shcherbinin, E. V. 1989 *Electrically Induced Vortical Flows*. Kluwer Academic Publishers.

Bratukhin, Yu. K. & Maurin, L. M. 1967 Thermocapillary convection in a fluid filling a half-space. *J. Appl. Maths. Mech.* **31**, 605–608.

Burggraf, O. R. & Foster, M. R. 1977 Continuation or breakdown in tornado-like vortices. *J. Fluid Mech.* **80**, 685–704.

Dean, W. R. 1934 Note on the divergent flow of fluid. *Phil. Mag.* **18**, 759–777.

Drazin, P. G., Banks, W. H. H. & Zaturska, M. A. 1995 The development of Long's vortex. *J. Fluid Mech.* **286**, 359–377.

Drazin, P. G. & Reid, W. H. 1981 *Hydrodynamic Stability*. Cambridge University Press.

Fernandez de la Mora, J., Fernandez Feria, J. & Barrero, A. 1991 Theory of incompressible conical vortices at high Reynolds numbers. *Bull. Am. Phys. Soc.* **36**, 2619.

Foster, M. R. 1993 Nonaxisymmetric instability in slowly swirling jet flows. *Phys. Fluids* A **5**, 3122–3135.

Gaster, M. A. 1962 A note on the relation between temporally-increasing and spatially-increasing disturbances in hydrodynamic stability. *J. Fluid Mech.* **14**, 222–224.

Georgiou, G. A. & Eagles, P. M. 1985 The stability of flows in channels with small wall curvature. *J. Fluid Mech.* **159**, 259–287.

Goldshtik, M. A. 1960 A paradoxical solution of the Navier–Stokes equations. *Appl. Math. Mech.* (*Sov.*) **24**, 610–621.

Goldshtik, M. A. 1990 Viscous flow paradoxes. *Ann. Rev. Fluid Mech.* **22**, 441–472.

Goldshtik, M. A., Hussain, F. & Shtern, V. N. 1991 Symmetry breaking in vortex-source and Jeffery–Hamel flows. *J. Fluid Mech.* **232**, 521–566.

Goldshtik, M. A. & Shtern, V. N. 1993 Axisymmetric hydromagnetic dynamo. *Prog. Astronaut. Aeronaut.* **149**, 87–102.

Govindarajan, R. & Narasimha, R. 1995 Stability of spatially developing boundary layers in pressure gradients. *J. Fluid Mech.* **300**, 117–147.

Gregory, N., Stuart, J. T. & Walker, W. C. 1955 On the stability of three dimensional boundary layers with application to the flow due to a rotating disk. *Phil. Trans. R. Soc. Lond.* A **248**, 155–199.

Hamel, G. 1916 Spiralförmige Bewegungen zäher Flüssigkeiten. *Jahresbericht Deutsch. Math. Verein.* **25**, 34–60.

Happel, J. & Brenner, H. 1986 *Low Reynolds Number Hydrodynamics* (4th printing). Martinus Nijhoff, Dordrecht.

Hooper, A. P., Duffy, B. R. & Moffatt, H. K. 1982 Flow of fluid of nonuniform viscosity in converging and diverging channels. *J. Fluid Mech.* **117**, 283–304.

Huerre, P. & Monkewitz, P. A. 1990 Local and global instabilities in spatially developed flows. *Ann. Rev. Fluid Mech.* **22**, 473–537.

Iooss, G. & Joseph, D. D. 1981 *Elementary Stability and Bifurcation Theory*. Springer.

Khorami, M. R. & Triveli, P. 1994 The viscous stability analysis of Long's vortex. *Phys. Fluids* **6**, 2623–2630.

Landau, L. D. 1944 On the exact solution of the Navier–Stokes equations. *Dokl. Akad Nauk SSSR* **43**, 299–301.

LONG, R. R. 1961 A vortex in an infinite viscous fluid. *J. Fluid Mech.* **11**, 611–623.

LOWSON, M. V. 1964 Some experiments with vortex breakdown. *J. R. Aeronaut. Soc.* **68** (641), 343.

PILLOW, A. F. & PAULL, R. 1985 Conically similar viscous flows. Part 1. Basic conservation principles and characterization of axial causes in swirling flows. *J. Fluid Mech.* **155**, 327–342.

PSHENICHNIKOV, A. F. & YATSENKO, S. S. 1974 Convective diffusion from localized source of surfactant. *Hydrodynamics* **5**, 175–181 (*Scientific papers of Perm University*, in Russian).

SAFFMAN, P. G. 1992 *Vortex Dynamics*. Cambridge University Press.

SCHLICHTING, H. 1933 Laminare Strahlausbreitung. *Z. angew. Math. Mech.* **13**, 260–263.

SCHLICHTING, H. 1979 *Boundary-Layer Theory*. McGraw-Hill.

SCHNEIDER, W. 1981 Flow induced by jets and plumes. *J. Fluid Mech.* **108**, 55–65.

SCHNEIDER, W., ZAUNDER, R. & BOHM, H. 1987 The recirculatory flow induced by a laminar axisymmetric jet issuing from a wall. *Trans. ASME* I: *J. Fluids Engng* **109**, 237–241.

SERRIN, J. 1972 The swirling vortex. *Phil. Trans. R. Soc. Lond.* A **271**, 325–360.

SHTERN, V. 1995 Cosmic jets as a pump for the magnetic field. *Phys. Lett.* A **206**, 96–100.

SHTERN, V. & BARRERO, A. 1995*a* Bifurcation of swirl in liquid cones. *J. Fluid Mech.* **300**, 169–205.

SHTERN, V. & BARRERO, A. 1995*b* Instability nature of the swirl appearance in liquid cones. *Phys. Rev.* E **52**, 627–635.

SHTERN, V. & HUSSAIN, F. 1993 Azimuthal instability of divergent flows. *J. Fluid Mech.* **256**, 535–560.

SHTERN, V. & HUSSAIN, F. 1994 Bifurcation cascade in a diverging flow. In *Nonlinear Stability of Nonparallel Flows*, pp. 449–458. Springer.

SHTERN, V. & HUSSAIN, F. 1996 Hysteresis in swirling jets. *J. Fluid Mech.* **309**, 1–44.

SHUSSER, M. & WEIHS, D. 1995 Stability analysis of source and sink flows. *Phys. Fluids* **7**, 25–32.

SOZOU, C. 1971 On fluid motion induced by an electric current source. *J. Fluid Mech.* **46**, 633–644.

SOZOU, C. 1992 On solution relating to conical vortices over a plane wall. *J. Fluid Mech.* **244**, 633–644.

SQUIRE, H. B. 1952 Some viscous fluid flow problem. 1. Jet emerging from a hole in a plane jet. *Phil. Mag.* **43**, 942–945.

TAYLOR, G. I. 1950 The boundary layer in the converging nozzle of a swirl atomizer. *Q. J. Mech. Appl. Maths* **3**, 129–139.

THOMPSON, J. 1855 On certain curious motions observable at the surfaces of wine and other alcoholic liquors. *Phil. Mag.* (4), **10**, 330–333.

WANG, C. V. 1991 Exact solutions of the steady-state Navier–Stokes equations. *Ann. Rev. Fluid Mech.* **23**, 159–177.

YATSEEV, V. N. 1950 On a class of exact solutions of the viscous fluid motion equations. *Sov. Phys., J. Exp. Theor. Phys.* **20**, 1031–1034.

YIH, C.-H., WU, F., GARG, A. K. & LEIBOVICH, S. 1982 Conical vortices: A class of exact solutions of the Navier–Stokes equations. *Phys. Fluids* **25**, 2147–2157.